Physica D 417 (2021) 132832

Contents lists available at ScienceDirect

Physica D

journal homepage: www.elsevier.com/locate/physd

Rayleigh–Taylor instability with gravity reversal

D. Livescu [a,*], T. Wei [b], P.T. Brady [a]

[a] Los Alamos National Laboratory, NM, USA
[b] New Mexico Tech, NM, USA

ARTICLE INFO

Article history:
Received 6 July 2019
Received in revised form 5 November 2020
Accepted 14 December 2020
Available online 27 December 2020

Keywords:
Direct Numerical Simulations
Turbulent mixing
Rayleigh–Taylor instability

ABSTRACT

We present results from Direct Numerical Simulations (DNS) of Rayleigh–Taylor instability at Atwood numbers up to 0.9. After the layer width had developed substantially, additional branched simulations have been run under reversed and zero gravity conditions. We focus on the modifications of the mixing layer structure and turbulence in response to the acceleration change. After the gravity reversal, the flow undergoes a complex transient process in which the vertical mass flux changes sign multiple times and, consequently, the buoyancy term in the turbulent kinetic energy transport equation changes its role back and forth from production to destruction. This behavior is examined in detail using the turbulent kinetic energy and mass flux transport equations and time instances when the vertical mass at the centerline crosses zero and reaches local minima and maxima. While the transient process significantly affects the flow anisotropy at all scales, other turbulence characteristics, like the alignment between the vorticity and eigenvectors of the strain rate tensor, retain their fully developed turbulence behavior in the interior of the layer. In addition, after the gravity reversal, the edges of the layer also exhibit characteristics closer to those of the turbulent interior, even as the fluids become more mixed. None of these changes affects the mean density profile, which still collapses among various cases. Such significant changes in some turbulence quantities and not others are difficult to capture with existing turbulence models.

1. Introduction

Classical Rayleigh–Taylor instability (RTI) [1–3] is generated at the interface between two different density fluids in the presence of a constant acceleration pointing from the heavy to the light fluid. The interface between the two fluids is unstable to any perturbation with a wavelength larger than the cutoff due to surface tension (for the immiscible case) or mass diffusion (for the miscible case). Thus, small perturbations of the initial interface grow, interact nonlinearly, and lead to turbulence. In most practical cases, RTI manifests itself as an extremely complex process, due to a multitude of factors, among which are large density differences, compressibility, temperature distribution, surface tension and other interfacial phenomena for the immiscible case or mass diffusion for the miscible case, molecular transport variations, geometrical and finite boundary effects, specific plasma and magnetic field properties, and so on. Flows featuring RTI-type growth of instabilities can be found in several important natural phenomena and applications, for example, in supernova explosions and X-ray bursts in neutron stars [4,5]; the solar corona [6,7]; Earth's oceans, atmosphere, and mantle [8]; quantum plasma; combustion [9]; inertial, magnetic, or gravitational confinement fusion [10–12]; sonoluminiscence [13], etc.

A useful limiting case, which isolates the basic instability from compressibility effects, considers two miscible incompressible fluids with different molar masses. The governing equations can be derived from the fully compressible Navier–Stokes equations under the assumption of an infinite speed of sound [14,15] or by directly assuming that the two fluids maintain constant densities [16]. We refer to this limit with large molar mass or density ratio (the non-Boussinesq case) as incompressible variable density (VD). Since the acoustic waves are filtered out for the VD equations, DNS at larger resolutions compared to the compressible case become feasible, which implies larger Reynolds and Atwood numbers [4,17]. Here, we consider RTI in the VD limit. VD equations have been used for DNS of RTI in Refs. [4,17–21].

The strength of the non-Boussinesq effects has traditionally been estimated using the Atwood number, $A = \frac{\rho_H - \rho_L}{\rho_H + \rho_L}$, where ρ_H, ρ_L are densities of the heavy and light fluids, respectively. The Boussinesq approximation corresponds to $A \to 0$ and a value of 0.05 is usually taken to define this limit. However, in many practical applications, $A \gg 0.05$, for example $A \sim 0.9$ in Inertial Confinement Fusion (ICF) [10,11] and $A \sim 0.85$ for hydrogen burning. The development of the instability and the mixing itself are fundamentally different at high and low A. Thus,

* Corresponding author.
E-mail address: livescu@lanl.gov (D. Livescu).

https://doi.org/10.1016/j.physd.2020.132832

the RTI mixing layer becomes asymmetric, rougher, and faster growing on the light-fluid side (showing so-called spikes) and smoother and slower growing on the heavy-fluid side (showing so-called bubbles) [22,23]; turbulence intensities are larger in light-fluid regions than heavy-fluid regions [24,25]; and mixing is asymmetric, with pure heavy fluid reaching larger depths from the layer edge than pure light fluid [14,15,19]. These asymmetries have also been explored in experimental studies [26–29].

In many practical applications, the driving acceleration changes in time or even reverses sign. For example, in ICF, shock waves can bounce back and forth from the center of the target, leading to complex acceleration histories at the material interfaces. RTI configurations with time varying acceleration, including changes in sign, have been studied both experimentally and in numerical simulations [30–35] and references therein; however, much less is known about the physics of the flow compared to the classical RTI. Time varying acceleration can also provide a mechanism for suppressing the instability [35], which is of interest in applications such as ICF.

However, the long time response of the flow to a change in acceleration has not been examined. In particular, the transients that appear after this change may pose significant challenges to turbulence models. In order to better understand the variable acceleration effects on the instability development and turbulence properties, we are focusing on the flow response to reversing or setting the acceleration to zero in the turbulent stage of the classical RTI. The latter is related to the Richtmyer–Meshkov instability, when the two fluids are subjected to an impulsive acceleration, e.g. due to a shock wave. To also examine the non-Boussinesq effects, we present detailed results from high resolution Direct Numerical Simulations of Rayleigh–Taylor instability, in the incompressible VD limit, at Atwood numbers of 0.5, 0.75 and 0.9. We contrast three configurations: (a) classical RTI with forward gravity (RTI+), (b) reversed gravity (RTI−) and (c) gravity set to zero (RTI0). Part of the preliminary results from these simulations has been presented in Refs. [17,36]. Here, we present the corresponding finalized results.

The paper is organized as follows: Section 2 presents the governing equations and numerical approach. Results concerning the flow development and turbulence structure are discussed in Section 3. Mixing layer width, growth rate, light/heavy fluid sides asymmetry, kinetic energy, mass flux and Reynolds number variations are addressed first. This is followed by a discussion of density PDF, lengthscales associated with buoyancy and turbulence, and Reynolds stress anisotropy at large and small scales. To explain the transient behavior of the flow after the gravity reversal, the transport equations for the turbulent kinetic energy and mass flux are considered. The discussion ends with an examination of the alignment between vorticity and eigenvectors of the strain rate tensor after the change in gravity. Finally, the conclusions of the paper are given in Section 4.

2. Governing equations, simulation cases, and numerical method

The incompressible VD equations can be derived from multi-species fully compressible Navier–Stokes equation as the infinite speed of sound limit [14,15], or by assuming that the fluids maintain constant microscopic densities [16,37]. The former derivation uses the energy equation consistently, while the latter simply neglects it in the incompressible limit. For the binary case, these equations are:

$$\frac{\partial}{\partial t}\rho + (\rho u_j)_{,j} = 0 \tag{1}$$

$$\frac{\partial}{\partial t}(\rho u_i) + (\rho u_i u_j)_{,j} = -p_{,i} + \tau_{ij,j} + \rho g_i \tag{2}$$

$$u_{j,j} = -\mathcal{D}(ln\rho)_{,jj} \tag{3}$$

The viscous stress is Newtonian with

$$\tau_{ij} = \rho\nu_0[u_{i,j} + u_{j,i} - \frac{2}{3}u_{k,k}\delta_{ij}] \tag{4}$$

Eqs. (1)–(2) are the usual continuity and momentum transport equations for compressible flows, with p representing only the dynamic pressure component [38]. The limiting process removes the pressure and temperature gradient effects, so that the diffusion operator becomes Fickian in the resulting incompressible equations. Since no other assumption is imposed, the resulting equations are non-Boussinesq. Thus, the density appears in the momentum equations and the divergence of velocity is not zero; the energy equation as well as the species transport equations leads to a formula for the velocity divergence in terms of the derivatives of the density field.

In Eqs. (1)–(3), the independent variables are the time t and space variables, x_i, in direction i, u_i is the velocity component in direction i, ρ is the mixture density, p is the dynamic pressure and g_i are the components of the gravitational acceleration, $\vec{g} = (0, 0, -g)$. The kinematic viscosity, $\nu_0 = \mu/\rho$, and mass diffusion coefficient, $\mathcal{D}$, are assumed constant and uniform in space. Note that, in general, the dynamic viscosity, μ, is a weaker function of density than linear; the assumption ν_0 constant ensures a uniform Schmidt number, $Sc = \frac{\nu_0}{\mathcal{D}}$ throughout the flow. A discussion on additional choices for the transport coefficients variations are provided in Ref. [15].

The equation of state for a binary mixture of ideal gases reduces in the infinite speed of sound limit to a diagnostic equation for the mass fractions of the two fluids [14,15]:

$$\frac{1}{\rho} = \frac{Y_H}{\rho_H} + \frac{Y_L}{\rho_L} \tag{5}$$

where the heavy and light fluid mass fractions, Y_H and Y_L, satisfy $Y_H + Y_L = 1$, and the microdensities ρ_H and ρ_L of the pure heavy and light fluids are constant. For an ideal gas mixture, $\rho_l = p_0 W_l/(T_0\mathcal{R})$, where p_0 and T_0 are the background pressure and temperature, $\mathcal{R}$ is the universal gas constant, and W_l is the molar mass of species l. In the incompressible limit, the microdensities, ρ_l, become constant. Relation (5) can also be obtained by first assuming constant micro-densities and then requiring that the volume occupied by the mixture is the sum of the volumes of the two fluids [16]. Relation (5) implies that the mixing rule for the dynamic viscosity is $1/\mu = \frac{Y_H}{\mu_H} + \frac{Y_L}{\mu_L}$, where $\mu_H = \nu_0\rho_H$ and $\mu_L = \nu_0\rho_L$ are the dynamic viscosities of the pure heavy and light fluids, respectively.

To facilitate the comparison with previous studies, the results are scaled by the length scale L_0, velocity scale $U_r = \sqrt{AgL_0}$, time scale $t_r = \sqrt{L_0/(Ag)}$, and $\rho_0 = (\rho_H + \rho_L)/2$. As explained below, L_0 is chosen as a length scale characterizing the initial perturbation spectrum. For the simulations presented here, L_0 is also close to the most unstable wavelength of the linear problem. Using L_0, U_r, t_r, and ρ_0 for non-dimensionalization changes the governing equations such that g is replaced by $1/A$, ν_0 by $1/Re_0 = \nu_0/(L_0\sqrt{AgL_0})$, and $\mathcal{D}$ by $1/(Re_0 Sc)$.

Eqs. (1)–(3) have been used in several previous studies, e.g., Refs. [4,14,18,24,25,39]. If the densities of the two fluids are commensurate, then the mixture density is close to its average value, ρ_0, and Eqs. (1)–(3) lead to the Boussinesq approximation [15].

For the Rayleigh–Taylor problem, Eqs. (1)–(3) have periodic boundary conditions in the horizontal direction and slip wall conditions are applied in the direction of gravity.

2.1. Numerical methodology

All simulations presented here were performed with the CFDNS code [17,20], using sixth-order compact finite differences [40] in the vertical (non-periodic) direction and spectral differencing in the horizontal (periodic) directions. To account for the difference in accuracy between the compact finite differences scheme and the Fourier differentiation, the grid spacing is 25% smaller in the vertical direction. For a well resolved spectral simulation, $\eta k_{max} \geq 1.5$, where η is the Kolmogorov microscale and k the Nyquist wavenumber. This condition corresponds to a grid spacing of less than 2η. Requiring the compact difference method to produce less than 25% error in differentiating a mode with this same wavelength dictates that the grid spacing must be refined relative to that of the spectral method by a factor of 0.8 [20]. Most energy in the flow corresponds to larger wavelengths, for which the differentiation error decreases rapidly. Nevertheless, since the Kolmogorov microscale is not well defined for the flow considered here, extensive resolution studies were performed to verify that the solution was converged.

In all simulations, $Sc = 1$, and the dynamic viscosity is chosen such that the mesh Grashoff number, $Gr \equiv 2A/Fr^2 \Delta_h^3/\nu_0^2$, is below 1 (a value of 0.88 was used in simulations). Here, $\Delta_h = 2\pi/N$ is the mesh size in the horizontal direction, where N is the number of grid points, and the mesh size in the vertical direction is $\Delta_v = 0.8\Delta_h$. The values of the acceleration are discussed below.

The time integration was performed with a variable-time stepping third order predictor–corrector Adams–Bashforth–Moulton scheme coupled with a pressure projection method. The variable density equations lead to a variable coefficient Poisson equation for pressure:

$$\nabla \cdot \left(\frac{\nabla p}{\rho^{n+1}} \right) = -\Delta + \nabla \cdot \left[(\rho \vec{u})^* / \rho^{n+1} \right] \tag{6}$$

where the divergence of velocity at time step $n+1$, Δ, is calculated based on ρ^{n+1} (3), which is known. $(\rho\vec{u})^*$ denotes the momentum at the intermediate step, after the momentum equations are advanced without the pressure terms. Eq. (6) is solved in two steps, to ensure that no errors are introduced in mass conservation or baroclinic production of vorticity. Thus, the equation is split into an explicit equation for the gradient component of $\nabla p/\rho$, which is related to mass conservation, and an implicit equation for the solenoidal (curl) component of $\nabla p/\rho$, which is related to the baroclinic term in the vorticity equation [24,39].

First, the gradient component of $\nabla p/\rho$ (denoted by ∇q) is determined from:

$$\nabla^2 q = -\Delta + \nabla \cdot \left[(\rho \vec{u})^* / \rho^{n+1} \right] \tag{7}$$

with

$$\nabla q \cdot \vec{n}_\Gamma = \left[(\rho \vec{u})^* / \rho^{n+1} \right] \cdot \vec{n}_\Gamma \tag{8}$$

Here, $\vec{n}_\Gamma$ is the normal to the non-periodic boundary, which is in the vertical direction. After applying the Fourier transform in the horizontal directions, Eq. (7) becomes a second order ordinary differential equation, with Neumann boundary conditions. The equation is discretized using the compact finite differences formula corresponding to Neumann boundary conditions. This leads to a penta-diagonal linear system for the Fourier coefficients of q. At the boundaries, lower order schemes (by 2 compared to the central regions), were used. The linear system is solved using a fast direct solver. For Neumann boundary conditions, q can only be determined up to an arbitrary constant. Thus, q is set to zero at one of the boundaries and the corresponding equation in the linear system is removed.

An equation for the curl component of $\nabla p/\rho$ (denoted by $\vec{Q}$) can be constructed from the formula:

$$\nabla p = \rho^{n+1} (\nabla q + \vec{Q}) \tag{9}$$

by taking the curl twice to yield:

$$\nabla^2 \vec{Q} = \nabla \times \left[\nabla ln \rho^{n+1} \times \left(\nabla q + \vec{Q} \right) \right], \tag{10}$$

with

$$\vec{Q}|_\Gamma = 0. \tag{11}$$

Eq. (10) is solved iteratively, using the direct Poisson equation solver described above, with hybrid Fourier transforms/6th order compact finite differences used to evaluate the right hand side. Unlike the triply periodic case addressed in Refs. [24,39], a separate equation for the average of $\nabla p/\rho$ is not necessary. This average is included in the gradient component.

The solution algorithm is parallelized using a 3-D domain decomposition. We have derived a fully distributed algorithm for the corresponding fast direct solver [41]. As an alternative, one can use a serial penta-diagonal direct solver coupled with matrix transposes to arrange the data on an entire line to be on-processor. Such transposes require communications only in the direction of the transform (or derivative) on single lines of processors. The same matrix transposes are also used for the Fourier transforms. With this decomposition, the code ran efficiently on 131,072 compute cores on the IBM BG/Q Sequoia supercomputer at Lawrence Livermore National Laboratory.

2.2. Simulation cases

To explore the response in the turbulence and mixing characteristics to the change in acceleration in VD RTI and provide data for model development and testing, we have performed fully resolved simulations of Rayleigh–Taylor instability on grid sizes $1024^2 \times N_Z$ and Atwood numbers 0.5, 0.75, and 0.9. To improve computational efficiency, N_Z is increased as the layer develops. After the layer width had developed substantially, additional branched simulations have been run under reversed and zero gravity conditions. The branched simulations start at $t/t_r \approx 16$, 14.4, and 12.2, for $A = 0.5$, 0.75, and 0.9, respectively. The simulations are stopped before the results become affected by the domain size in the vertical direction. Preliminary results from these simulations were first reported in Refs [17,36]. Here, we present more detailed, further analysis of the simulations.

For all simulations, the density is initialized to follow an error function profile in the vertical direction, which is consistent to the solution to the pure diffusion equation:

$$\rho = 0.5\,(1 + Erf\,[Y_v z + \zeta(x,y)])\,(\rho_H - \rho_L) + \rho_L, \tag{12}$$

with the slope coefficient Y_v chosen such that at least 8 grid points lie across the initial mixing layer. The initial perturbation $\zeta(x,y)$ has a top hat spectrum with energy between wavenumbers 30 and 34, with the middle wavenumber ($\kappa = 32$) close to the most unstable mode of the linearized problem calculated using the diffusive growth rate based on Ref. [42]. Thus, the initial perturbation length scale used for normalization of the results is $L_0 = 2\pi/32 \approx 0.196$.

To be able to compare simulations with different Atwood numbers, the acceleration g is varied such that the reference time scale, t_r, is ≈ 0.16 for all Atwood numbers ($Ag \approx 7.62$ for all Atwood numbers). The resulting velocity scale is $U_r \approx 1.22$. The simulations are summarized in Table 1.

Table 1
Summary of the simulation cases discussed in the paper. RTI+, RTI−, and RTI0 denote the forward ($g > 0$), reversed ($g < 0$), and zero ($g = 0$) gravity cases, respectively.

A	Type	Start time, t_0, in t_r units	Final size
0.5	RTI+	0	$1024^2 \times 2304$
0.5	RTI−	16	$1024^2 \times 2304$
0.5	RTI0	16	$1024^2 \times 2304$
0.75	RTI+	0	$1024^2 \times 4608$
0.75	RTI−	14.4	$1024^2 \times 2304$
0.75	RTI0	14.4	$1024^2 \times 2304$
0.9	RTI+	0	$1024^2 \times 2304$
0.9	RTI−	12.2	$1024^2 \times 2304$
0.9	RTI0	12.2	$1024^2 \times 2304$

2.3. Nomenclature

In defining the turbulence quantities, capital Roman letters, overbars, and angle brackets are used to denote Reynolds averages, which are taken over the periodic directions (assumed homogeneous). Angle brackets are preferred for longer expressions while overbars are used for quantities named with Greek letters. Primes are used to denote fluctuations. The density weighted (Favre) averages are denoted with $\tilde{}$, and the corresponding fluctuations with double primes. Thus, the instantaneous velocity, density, pressure, and specific volume are decomposed as $u_i = U_i + u_i' = \tilde{U}_i + u_i''$, $\rho = \bar{\rho} + \rho'$, $p = P + p'$, and $v = V + v'$, respectively. Note that $\tilde{U}_i - U_i = u_i' - u_i'' = a_i$. The definitions for the normalized mass flux, a_i, Favre Reynolds stresses, R_{ij}, and turbulent kinetic energy, $\tilde{k}$ or TKE, total kinetic energy, E_K, and density specific volume covariance, b, are given below:

$$a_i = \frac{\langle u_i \rho \rangle}{\bar{\rho}} = -\langle u_i'' \rangle \tag{13}$$

$$R_{ij} = \langle \rho^* u_i'' u_j'' \rangle = \bar{\rho}\langle u_i u_j \rangle - \bar{\rho} a_i a_j + \langle \rho u_i u_j \rangle, \tag{14}$$

$$\tilde{k} = R_{kk}/(2\bar{\rho}) = (\langle u_i u_i \rangle - a_i a_i + \langle \rho u_i u_i \rangle / \bar{\rho})/2 \tag{15}$$

$$E_K = \langle \rho^* u_i^* u_i^* \rangle / 2 = (\bar{\rho}\tilde{U}_i\tilde{U}_i + \langle \rho^* u_i'' u_i'' \rangle)/2 = \bar{\rho}(\tilde{K} + \tilde{k}) \tag{16}$$

$$b = -\langle \rho v \rangle. \tag{17}$$

These quantities are encountered in moment closures (see Refs. [25,43,44]) and are useful for the turbulence discussion below.

2.4. Turbulence moments equations

A moment closure approach at the second order level for variable density turbulence requires modeled transport equations for the Favre turbulent kinetic energy, $\tilde{k}$, normalized mass flux, a_i, and density specific volume correlation, b, or, alternatively, mean specific volume, V [43]. The corresponding transport equations [25] are shown here for completeness and to facilitate the discussion below:

$$\frac{\partial}{\partial t}\bar{\rho}\tilde{k} + (\bar{\rho}\tilde{U}_j\tilde{k})_{,j} = a_i(P_{,i} - \bar{\tau}_{ij,j}) - R_{ij}\tilde{U}_{i,j} - \frac{1}{2}R_{iij,j} - \langle u_i(p\delta_{ij} - \tau_{ij})\rangle_{,j} + \langle pd \rangle - \langle \tau_{ij} u_{i,j} \rangle \tag{18}$$

$$\frac{\partial}{\partial t}(\bar{\rho}a_i) + (\bar{\rho}\tilde{U}_k a_i)_{,k} = bP_i + \bar{\rho}\langle v p_i \rangle - \bar{\rho} a_j(\tilde{u}_i - a_i)_{,j} + \frac{\bar{\rho}_{,j}}{\bar{\rho}}(\langle \rho u_i u_j \rangle - R_{ij}) + \bar{\rho}(a_i a_j)_{,j} - (\langle \rho u_i u_j \rangle_{,j} + \bar{\rho}\langle u_i d \rangle) \tag{19}$$

$$\frac{\partial}{\partial t} b + \tilde{U}_j b_{,j} = 2a_j b_{,j} - 2a_j(1+b)\frac{\bar{\rho}_{,j}}{\bar{\rho}} + \bar{\rho}\left(\frac{\langle u_j \rho v \rangle}{\bar{\rho}}\right)_{,j} + 2\bar{\rho}\langle v d \rangle \tag{20}$$

$$\frac{\partial}{\partial t} V + \tilde{U}_j V_{,j} = 2a_j V_{,j} + V\tilde{U}_{j,j} + \left(\frac{\langle u_j \rho v \rangle}{\bar{\rho}}\right)_{,j} + 2\langle v d \rangle \tag{21}$$

The equations above are general and describe the moments evolutions in a fully compressible flow, regardless of the equation of state. Only after the application of (3), they become specific to the VD case.

3. Results

In this section, flow characteristics related to layer growth and its asymmetry, as well as turbulent kinetic energy and mass flux, are compared among the forward, reversed, and zero gravity cases, for the three Atwood numbers considered here, i.e. $A = 0.5$, 0.75, and 0.9. In addition, kinetic energy equation budgets, length scales, anisotropy, and vorticity alignments are discussed in more detail for the $A = 0.75$ simulation. With some notable exceptions, it is shown that turbulence in the inner region of the mixing layer of all three Atwood numbers has similar properties with other turbulent flows like homogeneous turbulence – isotropic, shear, etc. – mixing layers, wakes, jets, boundary layers, while the highly intermittent edge regions do not. After the gravity changes, the flow undergoes a transient process with large scale oscillations on a slowly decreasing time scale. Turbulence kinetic energy alternates periods of growths and decay, corresponding to oscillations in the sign of the mass flux, which determines the sign of the buoyancy term in the turbulent kinetic energy transport equation. While the overall Reynolds number decreases significantly, turbulence in the inner region maintains its structure and the edge regions start to exhibit similar characteristics.

3.1. Overview of flow evolution

The global behavior of the layer after the gravity change can be inferred from Fig. 1, which shows the evolution of the layer width based on several measures. For the miscible case, there is no unique definition of the layer width, and Fig. 1 compares some commonly used measures. Thus, $h_{CC} = \int_{-\infty}^{\infty} X_p(\bar{\rho})dz$ is based on the maximum product, $X_p(\bar{\rho})$, in a fast reaction analogy [4,18,25]. Refs. [45–49] use the definition $h_b = \beta W = \beta \int_{-\infty}^{\infty} F_1 F_2 dz$ for the layer thickness on the bubble side, where F_1 and F_2 are the averages (over horizontal planes) of the volume fractions occupied by the two fluids. For the incompressible variable density case, $F_1 = \frac{\rho_H - \bar{\rho}}{\rho_H - \rho_L}$ and $F_2 = \frac{\bar{\rho} - \rho_L}{\rho_H - \rho_L}$ using formula (5). The factor β accounts for the diffuse variation of the volume fraction near the bubble edge of the layer (a value of 3 corresponds to linear variation) and changes with A. For A values of 0.5, 0.75, and 0.9 considered here, β is $\approx$ 3.3, 3.1, and 3.0, respectively. A variation of this definition based on the mass fractions (or mass concentrations) has been used in Refs. [50,51] as $h = 6\int_{-\infty}^{\infty} Y_1 Y_2 dz$. Fig. 1 shows the half-width, h_c, corresponding to this definition. The two other measures shown in Fig. 1 are the bubble and spike heights, h_{95_b} and h_{95_s}, defined as the distance between the original centerline and the locations where the mean density falls within 5% of the pure fluid values, i.e. $\bar{\rho} = \rho_H - 0.05(\rho_H - \rho_L)$ on the bubble side and $\bar{\rho} = \rho_L + 0.05(\rho_H - \rho_L)$ on the spike side.

After the gravity changes sign, the layer width continues to grow for a short time due to inertia. During this time, as shown below, the layer undergoes dramatic rearrangements of the fluid parcels. Then, the layer width decreases, followed by a small bounce back, before settling to a quasi-constant value. Such behavior has also been observed in previous coarse mesh simulations [33,34]. The transitory increase in the layer width, as explained in more detail below, is associated with transitory changes in the sign of the mass flux, which determines the sign of the production term in the turbulent kinetic energy equation

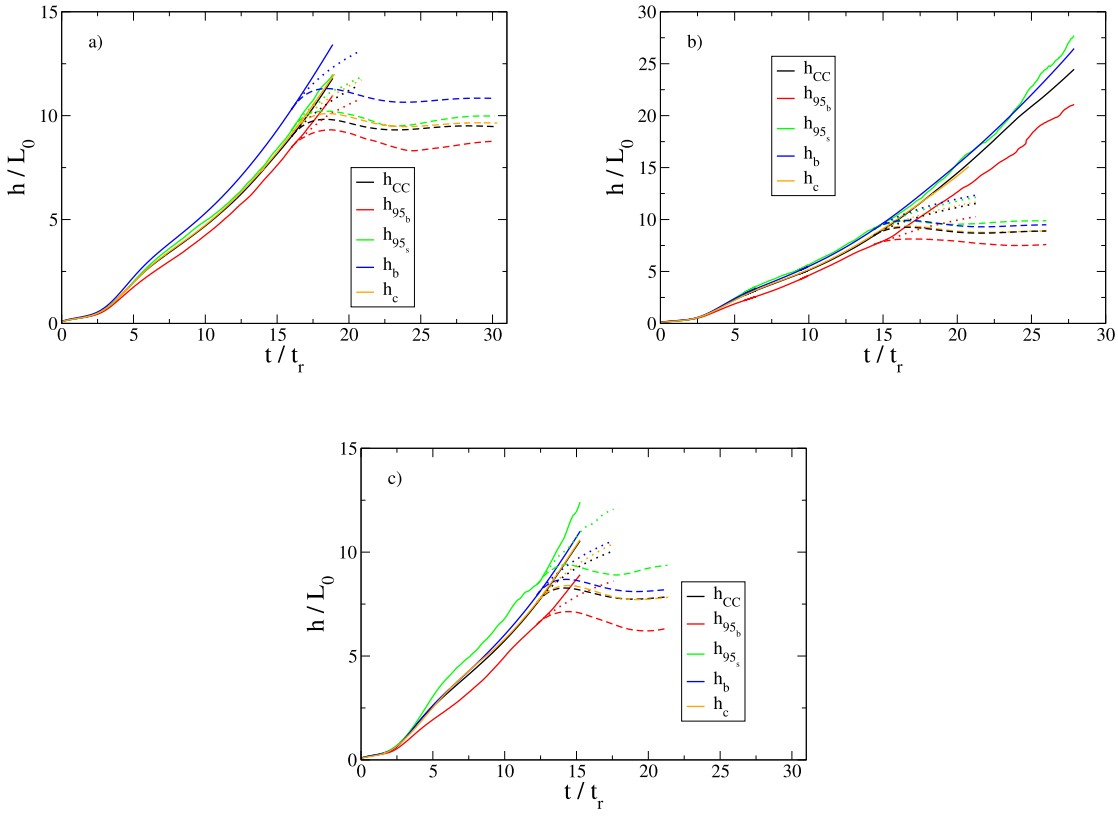

Fig. 1. The evolution of the layer width defined using a fast reaction analogy, h_{CC}, bubble side height defined based on volume fractions of the fluids, h_b, half-layer width defined based on the mass fractions of the fluids, h_c, and the bubble and spike heights, h_{95_b} and h_{95_s} for (a) $A = 0.5$, (b) $A = 0.75$, and (c) $A = 0.9$. See definitions in the main text. The main simulations (forward gravity or RTI+), shown with continuous lines, are branched into additional simulations with zero gravity (RTI0), shown with dotted lines, and reversed gravity (RTI−), shown with dashed lines.

(18), as described below. The process is further complicated by the local density inversions associated with the complex structure of the layer, which lead to secondary RT instabilities until the local stratification becomes stable. On the other hand, the zero gravity layer width continues to grow indefinitely, as expected.

While the overall differences among h_{CC}, h_b, and h_c are not very large, it is instructive to examine the variation across the layer of the corresponding integrand, $X_P(\bar{\rho})$, βW, and $3W_V$. Using formula (5), it can be shown that

$$W = \frac{\rho_L \rho_H}{(\rho_H - \rho_L)^2} \left(1 - \frac{\bar{\rho}}{\rho_H}\right) \left(\frac{\bar{\rho}}{\rho_L} - 1\right) \tag{22}$$

and

$$W_V = \frac{\rho_L \rho_H}{(\rho_H - \rho_L)^2} (1 - V\rho_L)(V\rho_L - 1)\,. \tag{23}$$

Fig. 2 shows that $X_P(\bar{\rho})$ and βW collapse relatively well for different Atwood numbers on the bubble side, while W_V shifts the entire profile to the spike side, as the mass fraction biases regions with small amounts of heavy fluid for larger Atwood numbers. Since h_b has been widely used in previous studies to scale the vertical variation, we use this width as well for the results presented in this paper.

Although certain classes of initial conditions (e.g. if long wavelengths are present in the initial perturbation [17,52]) may have a long lasting influence on the growth rate, it is generally agreed that at long times, if the turbulence growth is unrestricted, the turbulent mixing layer grows quadratically in time [4,25,53,54]:

$$h = \alpha A g t^2 + s\sqrt{\alpha A g h_0}\, t + h_0. \tag{24}$$

The quadratic growth has been known for a long time as a dimensionally consistent result confirmed by experimental data [3,

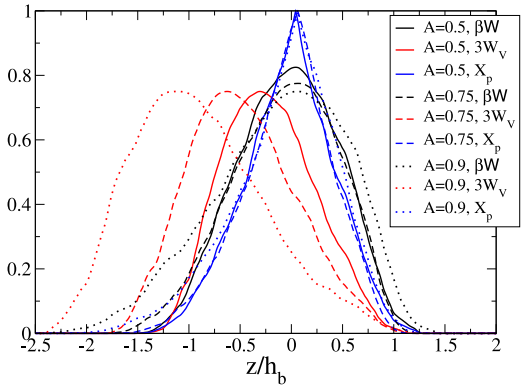

Fig. 2. The vertical variation of $X_p(\bar{\rho})$, βW, and $3W_v$, which enter the definitions of h_{CC}, h_b, and h_c, respectively, for the RTI+ cases with $A = 0.5$, 0.75, and 0.9 at $t/t_r \approx 16$.

45,55]. In terms of the scales defined in Section 2, the leading order term becomes $h/L_0 \sim \alpha(t/t_r)^2$. Although, asymptotically, the leading order term in Eq. (24) should dominate, the onset of self-similarity of the mixing layer width growth occurs much earlier and the lower order terms in Eq. (24) need to be properly accounted for. Ref. [4] used a formula consistent with the underlying self-similar differential equation for h [54],

$$\alpha = \frac{\dot{h}^2}{4Agh}. \tag{25}$$

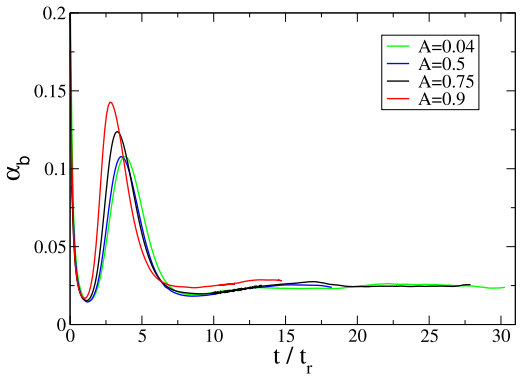

Fig. 3. The evolution of the growth rate for the RTI+ runs with $A = 0.5$, 0.75, and 0.9. For comparison, the growth rate results for the $A = 0.04$ case presented in Ref. [19] are also shown. The growth rate is calculated using formula (25), and h_b as the layer width, so it corresponds to the bubble side.

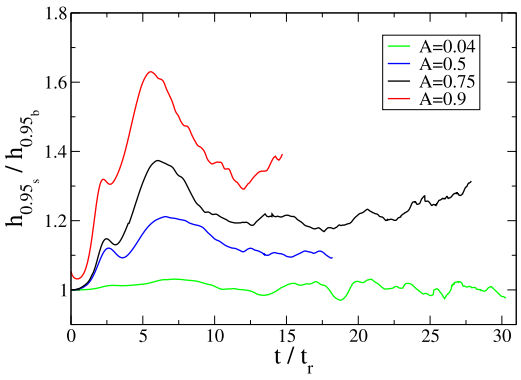

Fig. 4. The evolution of the spike to bubble height ratio for the RTI+ runs with $A = 0.5$, 0.75, 0.9, and $A = 0.04$ from Ref. [19].

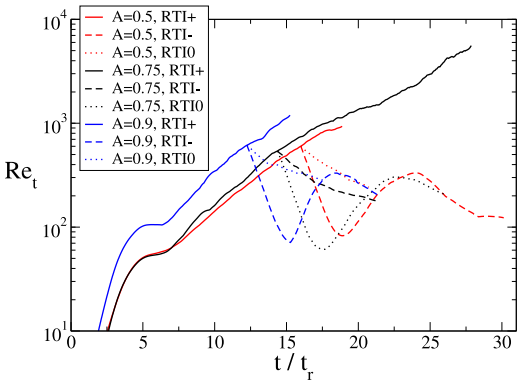

Fig. 5. The evolution of the turbulent Reynolds number at the location where TKE reaches its maximum value, for RTI+, RTI−, and RTI0 cases with different Atwood numbers.

Fig. 3 compares the evolution of the growth coefficient, α_b, for the bubble side for the cases considered here and the low Atwood number case ($A = 0.04$) from Ref. [19]. The growth coefficient is calculated using formula (25), with h replaced by h_b. The results are very close, with $\alpha_b \approx 0.025$, oscillating slightly between 0.022 and 0.027. The $A = 0.9$ results are slightly larger, but seem to also become close to the rest of the cases at the end of the simulation. The results are in general agreement with Ref. [49], corresponding to initial conditions with high wavenumber content. Thus, the values are lower than in earlier experimental results, but closer to newer experiments with better controlled initial perturbation spectrum [56,57].

After gravity is set to zero, the flow becomes anisotropic variable density decaying turbulence and has similarities with the Richtmyer–Meshkov instability (RMI). For RMI, the growth of the layer width, h, is well approximated by a power law of the type $h - h_0 = (t - t_0)^n$ [58], with the subscript "0" indicating the virtual origin. When a reshock is present, h_0 and t_0 are taken to correspond to the layer width and time at reshock [59]. Exponent values between 0.25 and 0.3 have been reported [60], with an intermediate stage where n is around 0.4 [59,61]. Using L_0 and t_r as length and timescales, h_b as the layer width, and the branch time and layer width as t_0 and h_0, the growth exponents obtained using a similar power law for the simulations presented here are $n \approx 0.67$, 0.62, and 0.55, corresponding to $A = 0.5$, 0.75, and 0.9, respectively. These exponents become established close to the branch time and seem to remain the same for the duration of the simulation. Thus, unlike the forward gravity case, there is a non-negligible Atwood number dependency on the growth rate after gravity is set to zero. In addition, these growth exponents are larger than those seen in RMI. While it is possible that the exponents may start decreasing for even larger simulations, they may also indicate a structural dissimilarity between the layer generated by impulsive and sustained accelerations, or they correspond to a certain region of the parameter space (e.g. Mach number, time to re-shock, initial perturbation spectrum), not yet explored in RMI.

Even as the growth on the bubble side seems to be little affected by the Atwood number for the runs presented here, the layer becomes increasingly asymmetric, and the spike side grows faster with A. To facilitate comparisons with previous studies, Fig. 4 shows the evolution of h_{95_s}/h_{95_b} for the Atwood numbers considered in this study and the $A = 0.04$ case from Ref. [19]. The ratio seems to approach a constant at late times ($t/t_r > 10$), whose value increases with A. The values shown in Fig. 4 are, again, in general agreement with Ref. [49], but lower than earlier experimental values, e.g. Ref. [23]. After the gravity change, the spike and bubble heights remain asymmetric (Fig. 1), with the ratio h_{95_s}/h_{95_b} approximately constant for the RTI0 cases, and presenting some oscillations correlated with the h oscillations from Fig. 1 for the RTI− cases (not shown).

The oscillations in the layer width following the gravity reversal can also be seen in the time evolution of the turbulent Reynolds number, shown in Fig. 5. The turbulent Reynolds number follows the expected decay for the RTI0 cases, but seems to oscillate without significant overall decay for the RTI−cases. This indicates that turbulence itself undergoes significant transitory changes, after the gravity reversal.

Thus, Fig. 6 shows that RTI0-cases start with a fast decrease of TKE, followed by a slight increase and then another decay. The increase in TKE can be partly associated with local density inversions present in the complex structure of the layer, which lead to secondary RT instabilities until the local stratification becomes stable. This is explored below using notions from stably stratified flow analysis. However, there is also a bounce of the whole turbulent layer, which can be seen using the turbulence moments equations presented in Section 2.4.

Eq. (18) shows that the term $a_i P_{,i}$ does not have a definite sign. When turbulence is established, this term is positive and represents the buoyancy production of turbulent kinetic energy [25,43]. However, the sudden change in the sign of gravity is reflected instantaneously only in the sign change of the mean pressure gradient. The mass flux continues to be negative for some time after the gravity reversal (Fig. 7), so that $a_i P_{,i}$ changes its role and becomes a destruction term. On the other hand, the buoyancy term in the mass flux transport equation (19) has a sign given

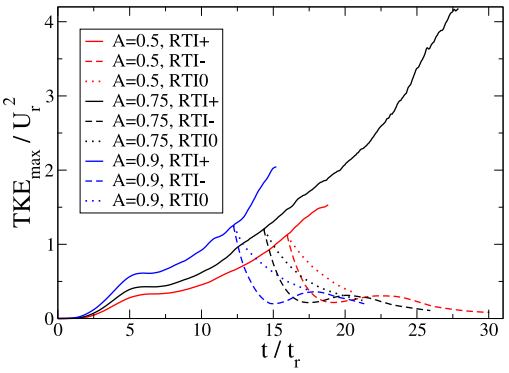

Fig. 6. The evolution of the maximum scaled turbulent kinetic energy (TKE) across the layer, RTI+, RTI−, and RTI0 cases with different Atwood numbers.

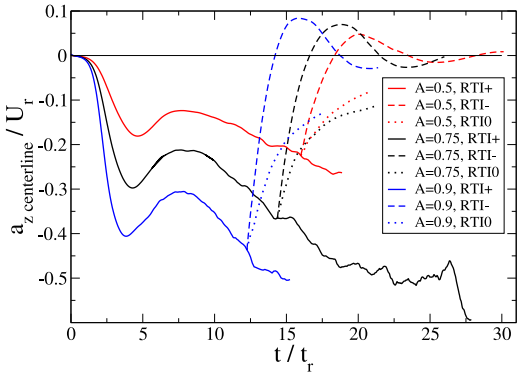

Fig. 7. The evolution of the mass flux at the centerline for RTI+, RTI−, and RTI0 cases with different Atwood numbers.

only by the mean pressure gradient, since the density specific volume correlation has definite sign. After the gravity reversal, this term also changes its role and becomes a destruction term. However, unlike the turbulent kinetic energy, the mass flux does not have a definite sign, and since turbulence does not decay on the time scale of the new buoyancy destruction term, mass flux itself overshoots and changes sign, as shown in Fig. 7. Nevertheless, $a_i P_{,i}$, which is now a buoyancy production term, is still a large term in the mass flux transport equation and the mass flux overshoots and reverses sign again. Fig. 7, which captures two additional zero crossings of the mass flux for $A = 0.5$ and $A = 0.75$ cases, shows that the interval between the subsequent zero crossings becomes smaller.

The normalized time instants corresponding to the zero crossings and local maxima/minima of the centerline mass flux are shown in Table 2, i.e. t_1 when the mass flux becomes zero for the first time, t_2, when the mass flux reaches its first positive peak, t_3, when the mass flux crosses zero the second time, t_4, when the mass flux reaches it first negative peak, and t_5, when the mass flux crosses zero the third time. In t_r time units, the interval between the zero crossings decreases from $\approx$ 5.15 to $\approx$ 4.7 for $A = 0.5$ and from $\approx$ 4.9 to $\approx$ 4.5 for $A = 0.75$. For comparison, the first zero crossing interval of the mass flux oscillations at $A = 0.9$ is ≈ 4.55, while the time interval between the gravity reversal and when the mass flux first becomes zero is ≈ 2.35, ≈ 2.2, and ≈ 2 for $A = 0.5$, 0.75, and 0.9, respectively.

The results presented in the rest of the paper focus on the $A = 0.75$ case for brevity. However, some of the $A = 0.5$ and $A = 0.9$ results are also shown, to emphasize the large A behavior. To facilitate the discussion of the flow physics, the variations across the layer are plotted at the time instants shown in Table 2.

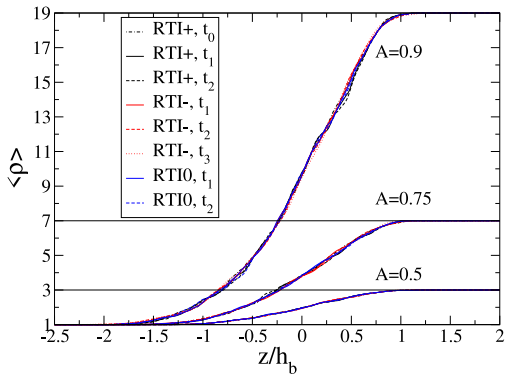

Fig. 8. Mean density profiles corresponding to RTI+, RTI−, and RTI0 cases with different Atwood numbers, at several time instants (see Table 2).

Table 2
Summary of the mass flux characteristic time instants for different Atwood numbers.

A	Time instant	t/t_r	$a_3\|_{z=0}$ behavior
0.5	t_0	16	Gravity reversal
0.5	t_1	18.35	First zero crossing
0.5	t_2	20.0	First positive peak
0.5	t_3	23.5	Second zero crossing
0.5	t_4	25.5	First negative peak
0.5	t_5	28.2	Third zero crossing
0.75	t_0	14.4	Gravity reversal
0.75	t_1	16.6	First zero crossing
0.75	t_2	18.8	First positive peak
0.75	t_3	21.5	Second zero crossing
0.75	t_4	23.4	First negative peak
0.75	t_5	26	Third zero crossing
0.9	t_0	12.2	Gravity reversal
0.9	t_1	14.2	First zero crossing
0.9	t_2	15.8	First positive peak
0.9	t_3	18.75	Second zero crossing
0.9	t_4	20.85	First negative peak

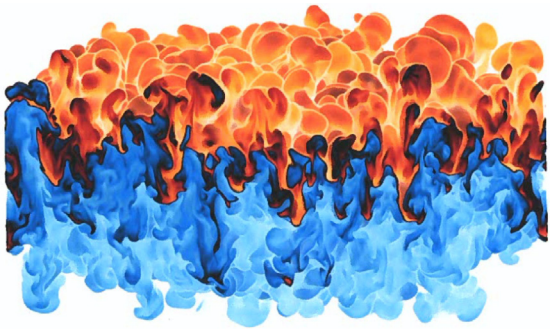

Fig. 9. Density field from the $A = 0.75$ simulation at t_0. Here, black represents fully mixed fluid, blue, light fluid, and yellow, heavy fluid.

3.2. Density field

To examine the modifications in the layer structure after the gravity change, in this section we focus on the density field. Fig. 8 shows that the mean density profiles collapse among the RTI+, RTI−, and RTI0 cases at the reference times defined above, giving little indication of the dramatic modifications in the underlying density field structure as the gravity changes. Moreover, the mean density variation remains linear in the inner region of the layer, retaining a fixed point at $z = 0$, similar to the classical RTI [25], and the edge regions remain asymmetric, with the profiles more elongated on the spike side. As shown in Ref. [25], this leads

to a host of asymmetries in many of the turbulence quantities. The collapse of the density profiles is consistent with the self-similarity of the layer growth discussed in the previous section. However, for the RTI− cases, the mixing layer evolution is clearly not self-similar, as reflected by the variations of the turbulent kinetic energy and mass flux.

Nevertheless, the variation of the density field shown in Figs. 9–12 clearly indicates that the mixing layer structure undergoes significant modifications after the gravity change. While the forward case, RTI+, exhibits more small scale activity as the layer grows from t_0 to t_3, the small scale structures are significantly damped for the RTI− case at t_3. The layer continues to grow for the RTI0 case with the small scale structures remaining similar for the three time instances shown. Interestingly, the asymmetry of the layer, with more elongated spike side, is maintained after the gravity change. The results for all three Atwood numbers are similar, and only the $A = 0.75$ results are shown here at several times and the $A = 0.9$ results at a late time, for brevity.

The changes in the density field can be highlighted be comparing its PDF across the layer. For the forward gravity case (Fig. 13a) the density PDF varies widely across the layer: at the bottom of the layer ($z < 0$) the PDF is spiked at the light fluid, at the top is spiked at the heavy fluid, while the transition is non-monotonic. Most of the RTI mix metrics are constructed from lower order moments of the density PDF and cannot capture this variation. Ref. [24] provides some rigorous bounds on the pure and mixed fluids based on the values of various mix metrics. In many cases, the bounds are far apart, clearly showing that such metrics are not useful in estimating the amounts of pure or mixed fluids.

In the forward gravity case, the interpenetration of the two fluids is highly irregular, giving rise to local density inversions. These inversions are quickly removed as the buoyancy force reverses sign (Fig. 13b) so that, at late times, the stratification becomes relatively uniform across the layer. This is shown by the much more narrow density PDF profiles, with a well defined peak. At each vertical position, the fluid becomes better mixed, indicative of a loss of internal structure of the layer. In addition, the width of the density PDF becomes narrower on the spike side, where the forward case exhibits more structure and roughness, indicating a more violent mixing process on this side following the gravity reversal.

Similar to the forward gravity case, in the zero gravity case (Fig. 13c), the density PDF at the centerline is not symmetrical, showing that some amount of pure heavy fluid reaches the centerline, but not the pure light fluid. Thus, the penetration distance of the pure heavy fluid is larger than that of the pure light fluid, a consequence of the mixing asymmetry in non-Boussinesq flows [17,24]. As the layer continues to grow due to the inertia of the individual fluid parcels, the mixing layer still develops and the density PDF demonstrates a rich internal structure. This behavior has similarities to the post re-shock evolution of the mixing layer in the Richtmyer–Meshkov instability [59].

3.3. Turbulence and buoyancy scales after gravity reversal

Following the gravity reversal, the mean stratification becomes stable, while the flows undergoes significant transients. To

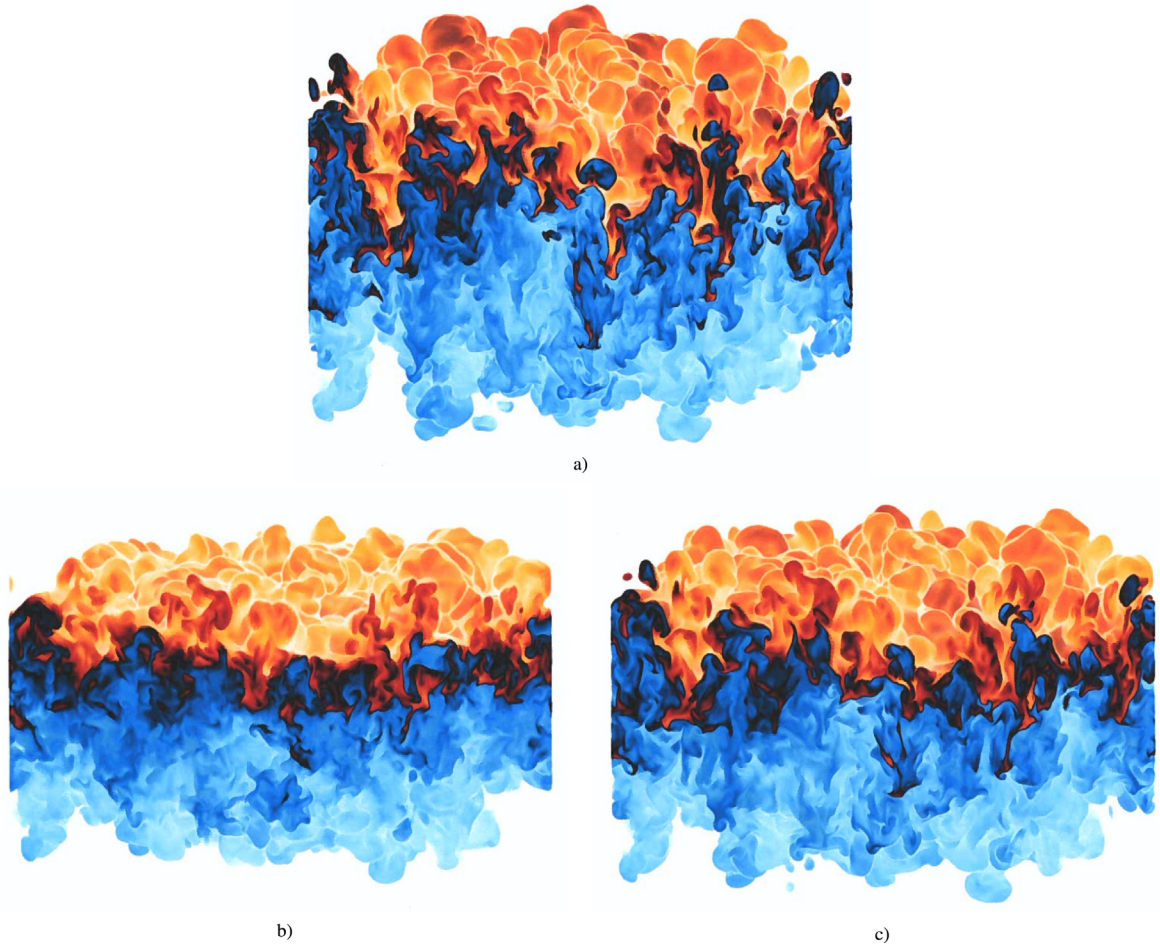

Fig. 10. Density field from the $A = 0.75$ simulations (a) RTI+, (b) RTI−, and (c) RTI0 at t_2 (see Table 2). Here, black represents fully mixed fluid, blue, light fluid, and yellow, heavy fluid.

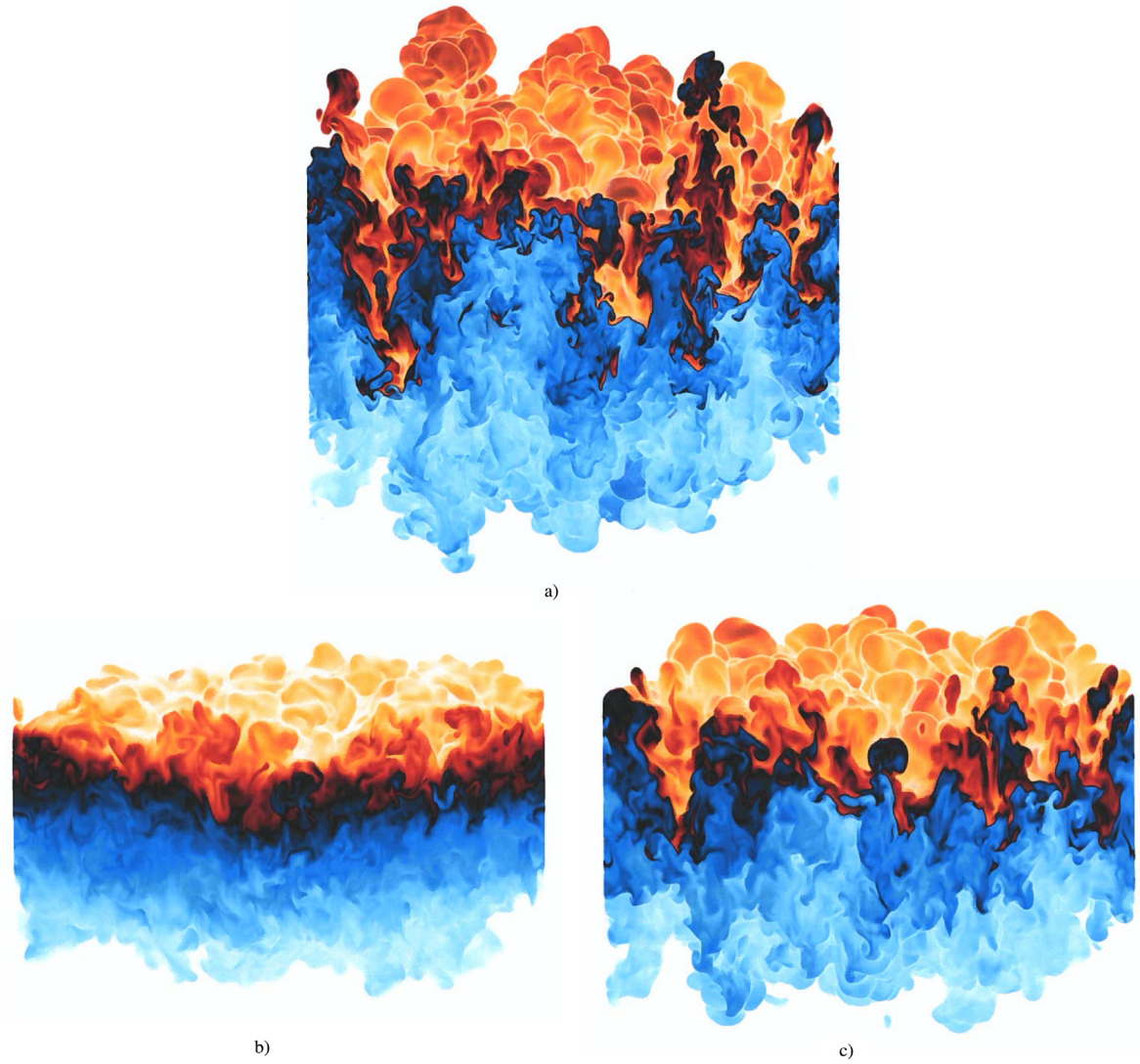

Fig. 11. Density field from the $A = 0.75$ simulations (a) RTI+, (b) RTI−, and (c) RTI0 at t_3 (see Table 2). Here, black represents fully mixed fluid, blue, light fluid, and yellow, heavy fluid.

understand the interplay between the buoyancy and turbulence, here we compare different scales across the layer for the RTI− cases at several time instances.

Fig. 14 shows that the turbulence integral scale ($L_t = \tilde{k}^{3/2}/\epsilon$) is comparable to half of the bubble height defined by h_b at the time of gravity reversal, t_0, for $A = 0.75$. However, the variation across the layer is asymmetric, with L_t values slightly larger on the spike side than on the bubble side. In the middle of the layer, the value of the turbulence integral scale corresponds roughly to wavenumber $\kappa = 8$. After the change in gravity, when the mass flux crosses zero the first time, L_t is significantly smaller ($L_t \approx 0.15h_b$) and exhibits less variation across the layer. Thus, at t_1, the gravity reversal appears as an efficient mixing mechanism for the large turbulence scales. Later, L_t, increases up to t_4, then decreases again at t_5, with larger values near the edges at the latest times, underlying the transients in the turbulence production mechanism. Fig. 14 also shows the variation across the layer at late times for $A = 0.5$ and 0.9 RTI− cases. The layer extent underlined by the L_t variation is similar on the bubble side for different Atwood numbers at corresponding times, while the extent clearly increases with A on the spike side. This is consistent with the other results presented above. Interestingly, in the middle of the layer, L_t values are relatively close for different Atwood numbers at corresponding times.

For stably stratified flows, the Ozmidov scale, $L_O = \left(\epsilon/N_{BV}^3\right)^{1/2}$, where $N_{BV}^2 = -|g|/\bar{\rho}d\bar{\rho}/dz$ is the Brünt–Väisällä frequency, defines the scale above which turbulence is inhibited by stratification. Due to the large variation of the mean density across the layer, here we use $\bar{\rho}$ in the definition of N_{BV}^2, instead of the usual definition with a constant background density. Fig. 15 shows that L_O is relatively constant across the layer, with larger values near the spike edge of the layer after the gravity reversal. At t_0, L_O is about $0.22h_b$ in the central region of the layer for $A = 0.75$, corresponding to wavenumber $\kappa = 16$. L_O continues to decrease after the gravity reversal, even during the transitory growth of the turbulent kinetic energy. While the layer extent on the spike side underlined by L_O variation clearly increases with A, L_O values in the interior of the layer are close for different A cases at corresponding times. At t_5, L_O reaches values around 0.045 in the interior of the layer, corresponding to wavenumber $\kappa = 75$.

The dominance of buoyancy over turbulence can also be seen in the variation of the dimensionless stratification parameter, $N_{BV}\ \tau$, where $\tau = \tilde{k}/\epsilon$, is the turbulence time scale. Thus, $N_{BV}\ \tau$ is relatively constant across most of the layer and larger than 1 most of the time Fig. 16. Unlike L_O, $N_{BV}\ \tau$ is not monotonic in time, and it first decreases after the gravity reversal. At t_1, $N_{BV}\ \tau$ is only slightly larger than one, a consequence of the violent response

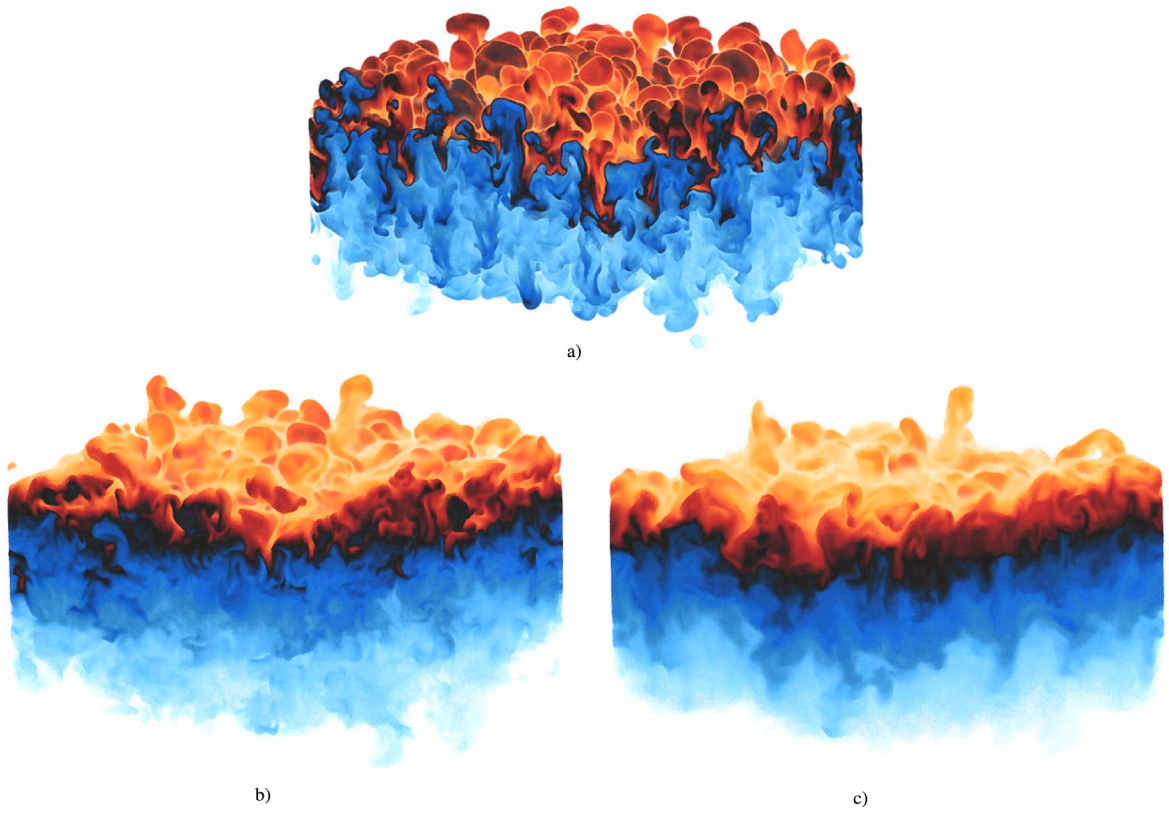

Fig. 12. Density field from the $A = 0.9$ RTI− simulation at (a) t_0, (b) t_1, and (c) t_2 (see Table 2). Here, black represents fully mixed fluid, blue, light fluid, and yellow, heavy fluid.

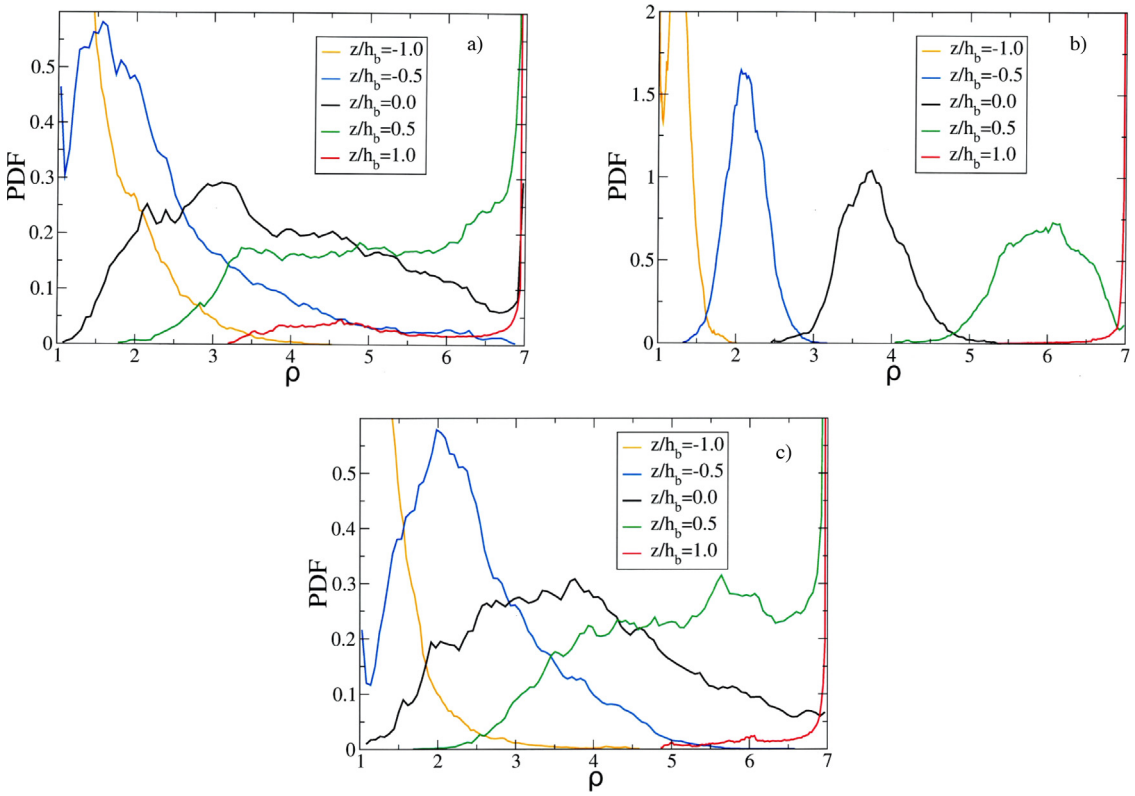

Fig. 13. Density PDF across the layer for the $A = 0.75$ simulations (a) RTI+, (b) RTI−, and (c) RTI0 at t_3 (see Table 2).

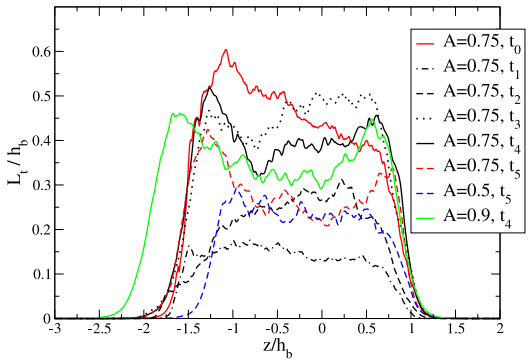

Fig. 14. Vertical variation of the turbulence integral scale, $L_t = \tilde{k}^{3/2}/\epsilon$ for RTI− cases at several times (see Table 2).

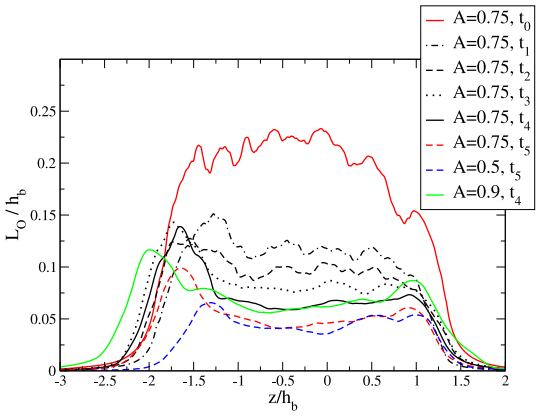

Fig. 15. Vertical variation of the Ozmidov scale, L_O, for RTI− cases at several times (see Table 2).

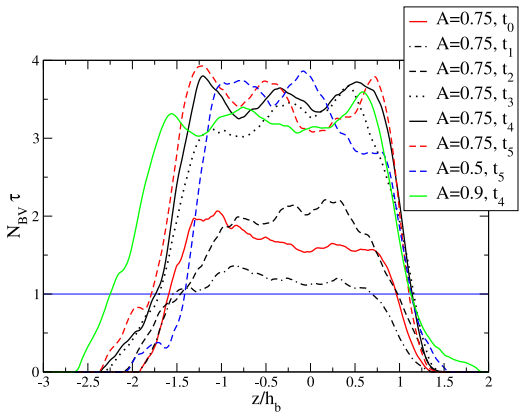

Fig. 16. Vertical variation of the dimensionless stratification parameter, $N_{BV}\ \tau$, for RTI− cases at several times (see Table 2).

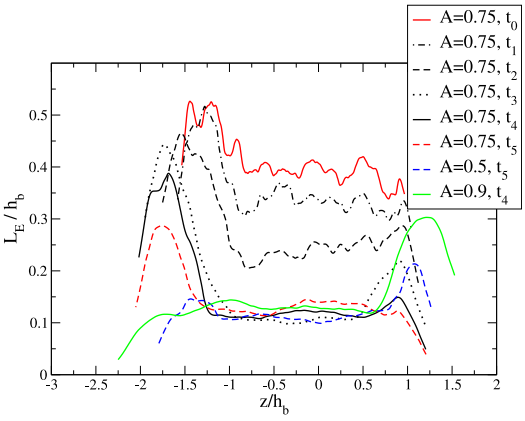

Fig. 17. Vertical variation of the Elisson scale, L_E, for RTI− cases at several times (see Table 2).

of the flow to the sudden change in gravity. It then continues to increase and seems to reach an asymptotic value between 3 and 4 at the latest times, with relatively little variation with the Atwood number.

The Elisson scale, $L_E = \langle \rho'^2 \rangle^{1/2}/|d\bar{\rho}/dz|$ is usually used as a surrogate to represent the Thorpe and eventually Ozmidov scale and, thus, estimate the turbulence dissipation from observations where this is not available. There is a lot of work in the literature on estimating the Elisson scale, including efforts to remove the contribution to the density fluctuations from the internal gravity waves. This decomposition is beyond the scope of the current paper, since the processes following the gravity inversion are highly transient and the density fluctuations may also be affected by additional physics. We merely note that L_E is also relatively constant throughout the interior of the mixing layer at all time instances shown in Fig. 17 and seems to reach an asymptotic value around 0.1 for all A cases studied here at late times. Thus, $L_E > L_O$ by a factor of around 2.

3.4. Large and small scale anisotropies

In the forward gravity case, it is known that the flow is anisotropic at large scales (e.g. [19,25,54,62]), which is a direct consequence of the anisotropic buoyancy production. The usual measure for this anisotropy is calculated based on the normal stresses. The Favre Reynolds stress anisotropy tensor is defined by:

$$b_{ij} = \frac{R_{ij}}{R_{kk}} - \frac{1}{3}\delta_{ij} \tag{26}$$

and b_{33} is the relevant large scale anisotropy measure for this flow. b_{33} is bounded by $-\frac{1}{3} \le b_{33} \le \frac{2}{3}$.

Fig. 18 shows that b_{33} variation at the centerline for the forward gravity cases convergences in the turbulent stage to ≈ 0.3, similar to the behavior at $A = 0.04$ (e.g. [25]). For this value, approximately 2/3 of the turbulent kinetic energy is concentrated in the vertical direction, so that $R_{33} \approx 4R_{11}$. After the gravity is set to zero, b_{33} decreases rapidly, but it seems to asymptote to a constant value of ≈ 0.15 for all A cases considered here. For this value, the vertical and horizontal kinetic energies are approximately the same, so that $R_{33} \approx 2R_{11}$. However, gravity reversal sets in an oscillatory behavior, with the troughs around zero (corresponding to isotropic energy distribution) and the peaks between 0.25 and 0.27. The first trough coincides with the first zero crossing of the mass flux for all three Atwood number cases. However, the subsequent oscillations no longer seem correlated with the mass flux behavior. Thus, the first peak of the b_{33} oscillations occurs earlier than t_3, while the second trough seems to occur later than t_5. While definitely the mass flux sign reversals and subsequent oscillation of the role of a_3P_3 term in the R_{11} transport equation between production and destruction are responsible for the time oscillations of centerline b_{33}, there are many more degrees of freedom in the flow, and these quantities are not fully correlated. Thus, as shown below, there is a large scale oscillation of the flow across the layer, as well as energy exchange among the normal stresses that varies with the scale.

Unlike the behavior observed at $A = 0.04$, Fig. 19 shows that b_{33} is no longer constant across the layer. This is not surprising,

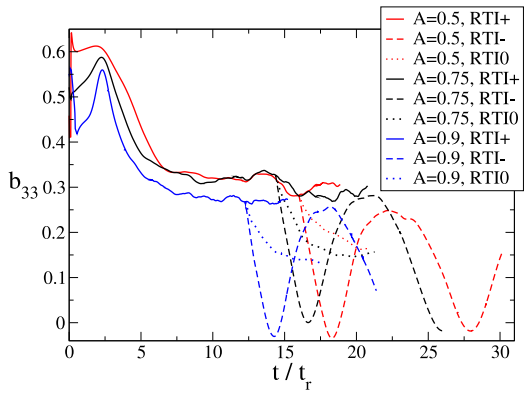

Fig. 18. Time evolution of b_{33} at the centerline for RTI+, RTI−, and RTI0 cases with different Atwood numbers.

since at higher A values it is expected that the asymmetries in the layer become significantly more pronounced. In fact, experimental evidence (e.g. [23]) suggests that the high A effects should become evident only for $A > 0.5$. Here, the results indicate larger levels of the normal stresses anisotropy on the spike side, that also seem to increase with A. After the gravity is set to zero, the large scale anisotropy decreases considerably across most of the layer, in the absence of the sustained reinforcement of the buoyancy force (Fig. 19a). Interestingly, b_{33} values in the inner region of the layer closer to the bubble side are approximately the same for all Atwood numbers considered here, for both RTI+ and RTI0 cases. However, the edges of the layer remain more anisotropic than the turbulent interior, as the turbulence is more efficient in mixing the flow than the highly intermittent, non-turbulent edge regions. This effect is clearly seen for the reversed gravity case at different time instances (Fig. 19b). While the centerline value of b_{33} reaches values close to zero repeatedly, the edge regions maintain relatively large levels of anisotropy.

In general, in high Reynolds number flows, the small scales become isotropic and decoupled from the large scales, since production mechanisms tend to be confined to large scales. However, our previous results [19,24,25] show that buoyancy production, even though it becomes much smaller than the nonlinear transfer in the spectral kinetic energy equation at high wavenumbers, has a significant effect on the smallest scales of the flow, in both classical RTI (up to $A = 0.5$) and an idealized, triply periodic, homogeneous Rayleigh–Taylor flow, provided that the flow is highly non-equilibrium, i.e. TKE production far exceeds TKE dissipation. If the Reynolds number is large enough, so that the viscous scales are well separated from the large scales, an inertial range can still develop, since buoyancy production decreases faster with the wavenumber than the nonlinear transfer. However, in the viscous range, there is a cancellation between the two largest terms in the spectral kinetic energy equation so that the buoyancy production, even though much smaller than these two terms, becomes, again, important. Thus, the largest and smallest scales remain anisotropic. This finding was also confirmed in a stationary, triply periodic buoyancy driven flow [39].

Obviously, such considerations are merely qualitative, even if supported by DNS data in multiple flows, and may change at much larger Reynolds number values. Nevertheless, given the size of the simulations analyzed here and those mentioned above, it is highly unlikely that such questions will be settled in the near future using direct simulations. Some answers might arrive sooner by means of spectral analysis (see for example Ref. [63,64]), especially in the Boussinesq limit, though the analysis is also complicated by the non-equilibrium nature of the flow regime where this effect has been seen. Here, we present the numerical results, which are consistent with previous observations, and speculate about their generality.

For variable-density flows, there is no unique way to define a kinetic energy spectrum. Both quadratic and non-quadratic forms have been used in previous studies, However, in order for the kinetic energy spectrum to develop an inertial range, the viscous effects need to be restricted to the small scales. Ref. [65] showed that for variable density turbulence, it is possible that certain quantities exhibit viscous effects at all scales, while others do not. In particular, using a coarse-grained filtering, they showed that filtered Favre turbulent kinetic energy has the property that viscous effects vanish at large scale for large enough Reynolds numbers for constant viscosity. There is no general formulation for arbitrary viscosity variations. Nevertheless, Ref. [66] extended the arguments to spectral representations and showed that a spectral kinetic energy definition based on the square of the momentum, $\langle|\rho^* u''/\sqrt{\bar{\rho}}|^2\rangle$ also has vanishing viscous contribution at sufficiently large Reynolds numbers, for constant viscosity. Here, we follow Ref. [66] and define the anisotropy as a function of scale as

$$b_{33}(\kappa) = \frac{E_{33}(\kappa)}{E_{ii}(\kappa)} - 1/3 \tag{27}$$

where the kinetic energy spectrum in direction j is calculated as $E_{jj}(\kappa) = \langle(\widehat{\rho^* u_j''})(\widehat{\rho^* u_j''})^\dagger\rangle/\bar{\rho}$ (no summation over j here), with $\widehat{\ }$ denoting the Fourier transform, † the complex conjugate, and the average is taken over spherical shells centered at wavenumber κ.

While there are some small differences compared to definitions based on spectral forms of the Favre Reynolds stresses (not shown), the results are consistent with previous results for the forward gravity case. Thus, Fig. 20 shows that in some intermediate range, which would correspond to an emerging inertial range, the anisotropy is smaller than at large and small scales. For the $A = 0.75$ zero gravity case (Fig. 20b), immediately after the gravity is set to zero, all scales feel the sudden change in the forcing. Thus, at t_1, there is a decrease in anisotropy at large scales and an increase at the very small scales. Later, as the flow evolves to t_2 and t_3, the large scale anisotropy remains relatively unchanged, while the small scale anisotropy decreases; this is expected for a decaying flow, when the Reynolds number continuously decreases.

However, $b_{33}(\kappa)$ behavior exhibits additional time oscillations for the RTI− case. After the gravity change, the qualitative remarks based on the cancellation between the viscous and nonlinear terms in the spectral kinetic energy evolution no longer hold, as all scales are affected by the transitory effects. Fig. 20c shows that the intermediate scale values do not change much, but the large scale anisotropy decreases immediately following the gravity reversal, then increases as turbulent kinetic energy is again generated by buoyancy production, and, finally, decreases to around zero as the mass flux reaches zero for the third time (t_5). The small scale behavior also changes in time, but in a different way than at large scales. The anisotropy at the smallest scales remains relatively large and seems to follow the sign of the mass flux. Thus, at t_2, $b_{33}(\kappa)$ has lower values at the far right of the spectrum, while at t_4, when buoyancy acts again as a production term, the small scale anisotropy becomes large. Although reversing gravity might represent an efficient mixing mechanism for the large scales, it seems the transient behavior following the change in gravity leads to a persistent small scale anisotropy. The results for the $A = 0.9$ RTI− case are similar (20d).

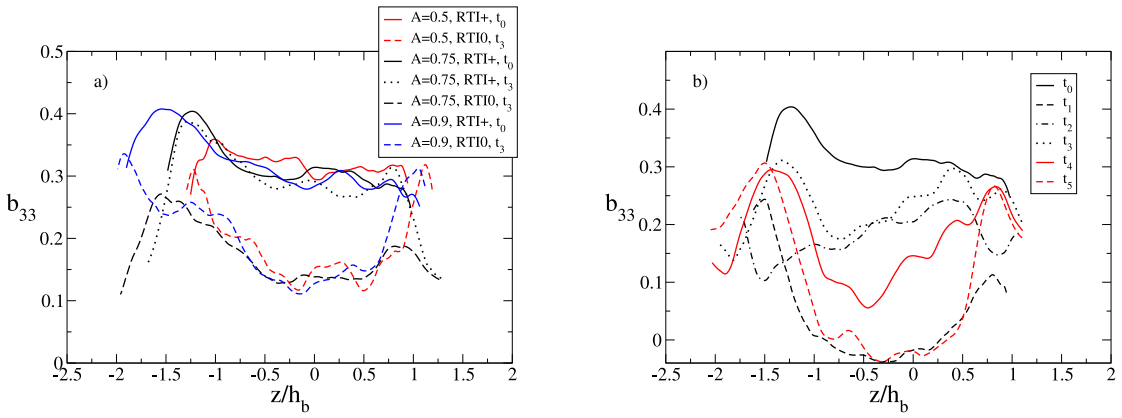

Fig. 19. Vertical variation of b_33 at the centerline for (a) RTI+ and RTI0 cases, $A = 0.5$, 0.75, and 0.9, at t_0 and t_2, and (b) $A = 0.75$ RTI− case at different times (see Table 2).

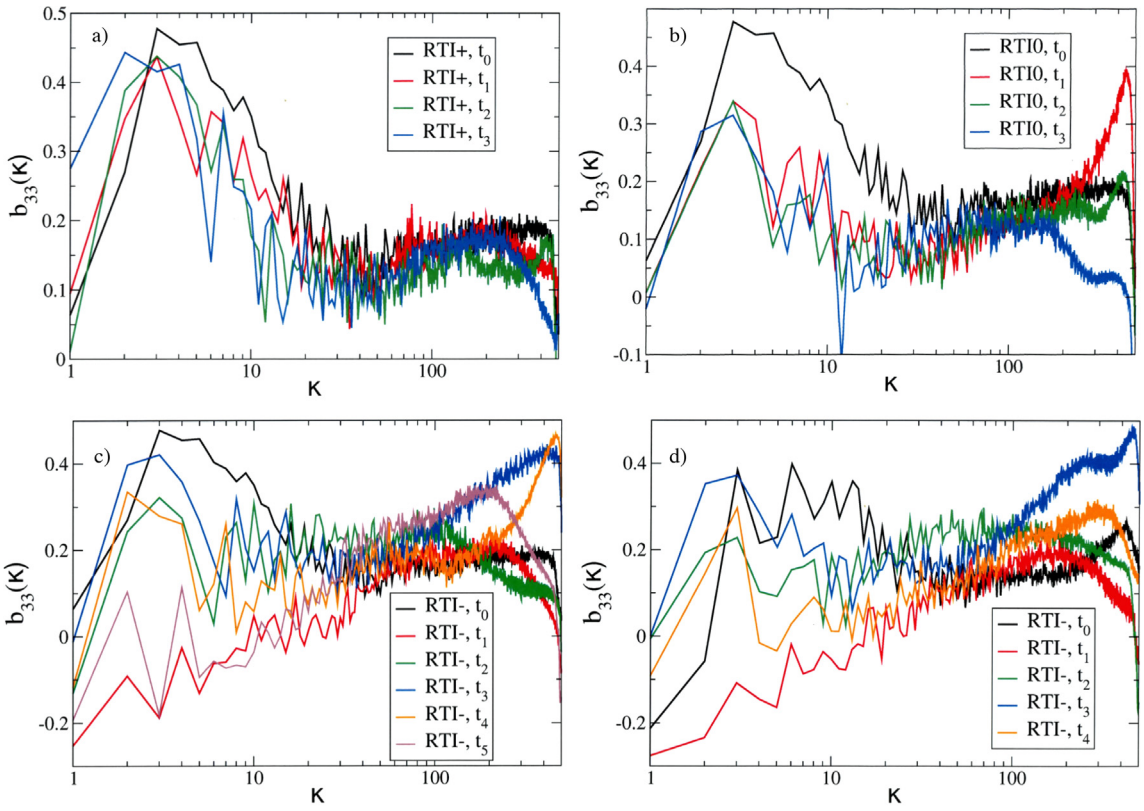

Fig. 20. Scale dependence of normal stresses anisotropy at the centerline for (a) RTI+, $A = 0.75$, (b) RTI0, $A = 0.75$, (c) RTI−, $A = 0.75$, and (d) RTI−, $A = 0.9$ at different times (see Table 2).

3.5. Turbulent kinetic energy and mass flux transport equations budgets

The transient behavior of the flow evolution for the RTI− case was associated above with the production terms in the turbulent kinetic energy and mass flux transport equations. In this section, the terms in these equations are examined at time instants t_2-t_4 for $A = 0.75$. For completeness, we first show the variation across the layer of the turbulent kinetic energy and mass flux in Figs. 21(a) and (b), respectively. For all time instants, both $\tilde{k}$ and a_3 peak on the spike side, consistent with previous studies (e.g. [19,25]). After the gravity reversal, the peaks move towards the centerline, but the spike side still exhibits more turbulence activity. While the results display the repeated change in the mass flux sign at the centerline, the mass flux remains positive at the mixing layer edges regions after the initial large transient. This is further discussed below.

Figs. 22 and 23 show the vertical variation of the non-negligible terms in the turbulent kinetic energy equation (18). The definitions of these terms for the current configuration, with periodic horizontal ("1" and "2") and non-periodic ("3") direction, are shown in the figure caption. At t_0 (Fig. 22a), the variation of the terms is similar to the results presented in Ref. [25], except for the buoyancy term *II*, which is negative for RTI−. This sudden change in the role of the buoyancy term from production to destruction of turbulent kinetic energy leads to rapid decrease in the turbulent kinetic energy immediately following the gravity

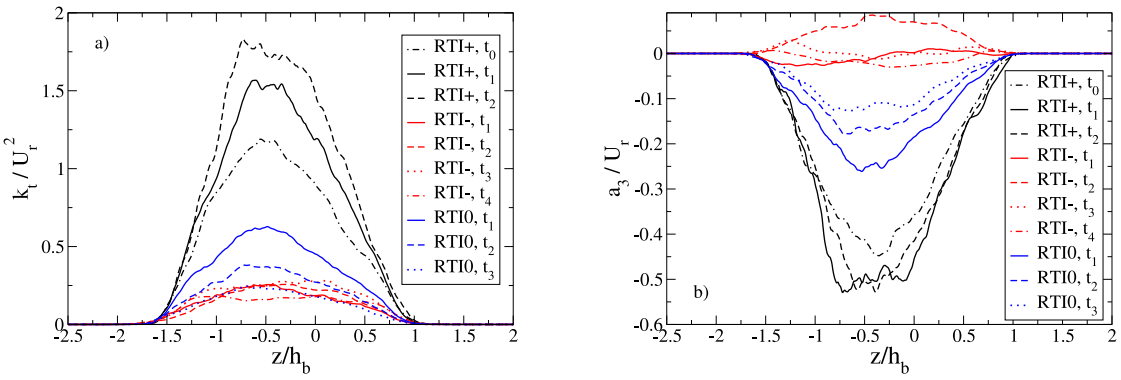

Fig. 21. Vertical variation of scaled (a) turbulent kinetic energy and (b) turbulent mass flux for the $A = 0.75$ RTI+, RTI−, and RTI0 cases at different times (see Table 2).

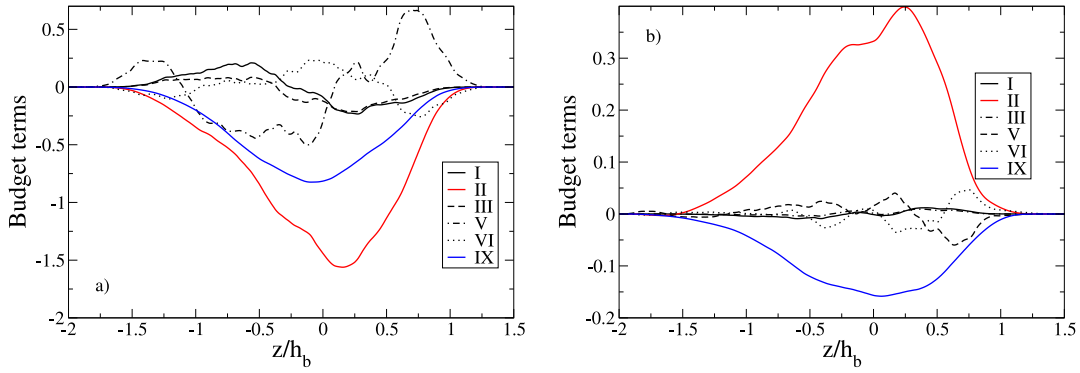

Fig. 22. Vertical variation of the non-negligible terms in the turbulent kinetic energy transport equation (18) for RTI− case with $A = 0.75$ at (a) t_0 and (b) t_2. The reference times are presented in Table 2. The definitions of the terms for the current configuration are $I = -(\tilde{\rho}\tilde{U}_3\tilde{k})_{,3}$, $II = a_3 P_{,3}$, $III = -R_{33}\tilde{U}_{3,3}$, $V = -1/2R_{ii3,3}$, $VI = -\langle u_3 p\rangle_{,3}$, $IX = -\langle \tau_{ij} u_{i,j}\rangle$. All terms are scaled by U_r^2/t_r. The transport terms are shown in black, buoyancy term with red, and dissipation term with blue lines, respectively.

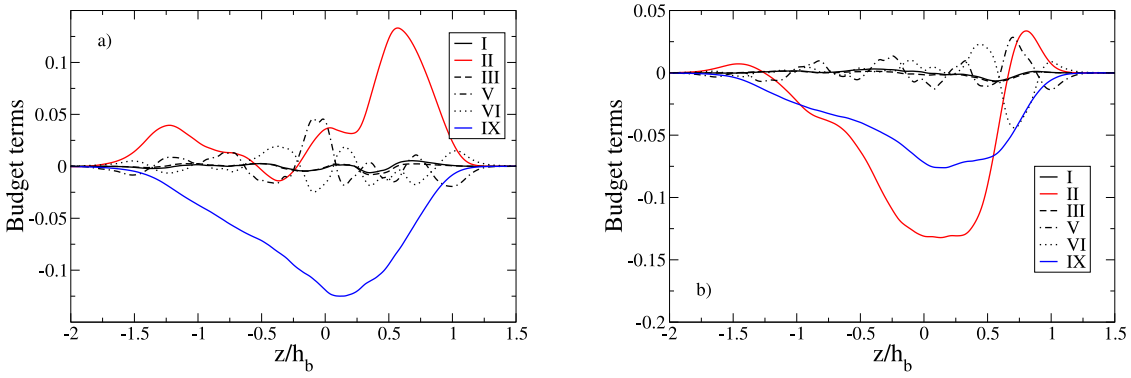

Fig. 23. Vertical variation of the non-negligible terms in the turbulent kinetic energy transport equation (18) for RTI− case with $A = 0.75$ at (a) t_3 and (b) t_4. The reference times are presented in Table 2. The definitions of the terms for the current configuration are shown in Fig. 22.

reversal. However, the other terms in the equation do not suddenly change, so that the layer still grows for a short time, as the pressure velocity correlation continues to transport energy from the interior to the edges of the layer. By t_2, (Fig. 22b), all transport terms become small, and the budget is dominated by the buoyancy and dissipation terms. At this time, since the turbulent mass flux has changed sign but the mean pressure gradient maintains the sign of the acceleration, the buoyancy term is positive and represents a production mechanism for the turbulent kinetic energy. Later, at t_3, Fig. 21b shows that the mass flux is small at the centerline, but still positive near the edges of the layer. Consequently, Fig. 23(a) shows that buoyancy continues to produce turbulent kinetic energy near the edges of the layer. At t_4, (Fig. 23b), the buoyancy term is again negative around the centerline, so it accelerates the decay of the turbulent kinetic energy in the central region of the layer. Nevertheless, buoyancy continues to generate kinetic energy at the very edges of the layer.

We now turn to the behavior of the terms in the vertical turbulent mass flux transport equation (19). Unlike the buoyancy term in Eq. (18), the buoyancy term in (19) maintains positive sign at all times following the gravity reversal (Figs. 24 and 25), as both b and mean pressure gradient maintain constant sign. However, since the mass flux itself changes sign, this term acts as a production or destruction mechanism. Term III is a destruction mechanism for the mass flux in the forward case, however, for

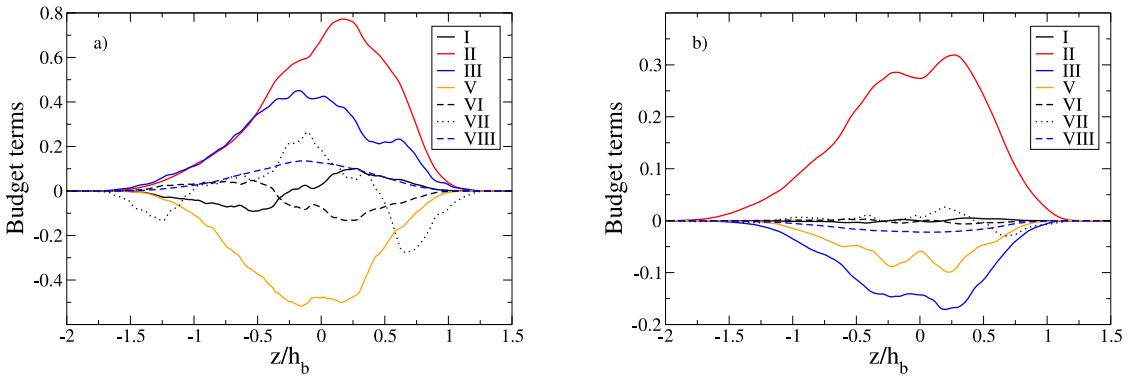

Fig. 24. Vertical variation of the non-negligible terms in the turbulent mass flux transport equation (19) for RTI− case with $A = 0.75$ at (a) t_0 and (b) t_2. The reference times are presented in Table 2. The definitions of the terms for the current configuration are $I = -(\bar{\rho}\tilde{U}_3 a_3)_{,3}$, $II = bP_{,3}$, $III = \bar{\rho}\langle vp_{,3}\rangle$, $V = \bar{\rho}_{,3}/\bar{\rho}(\langle \rho u_3^2\rangle - R_{33})$, $VI = \bar{\rho}(a_3^2)_{,3}$, $VII = -\langle \rho u_3 62\rangle_{,3}$, and $VIII = -\bar{\rho}\langle u_r u_{i,i}\rangle$. All terms are scaled by U_r. The transport terms are shown in black, buoyancy term with red, destruction term *III* with blue, and term *V* with yellow lines, respectively.

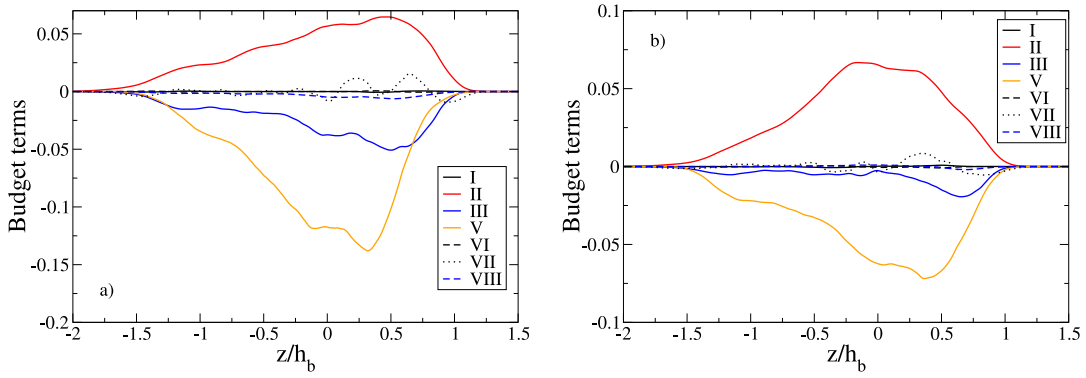

Fig. 25. Vertical variation of the non-negligible terms in the turbulent mass flux transport equation (19) for RTI− case with $A = 0.75$ at (a) t_3 and (b) t_4. The reference times are presented in Table 2. The definitions of the terms for the current configuration are shown in Fig. 24.

RTI− it can also act as a production term in different regions of the layer. Term V maintains constant negative sign, opposite to the buoyancy term, throughout the RTI− evolution. Even though the density PDF indicates a significant loss of structure for the density field, there are still pockets of less mixed fluid across the layer, so that b and, consequently, the buoyancy term are large enough to produce an overshoot and change in sign of the mass flux. Interestingly, the non-negligible constant sign term V is essential for the subsequent change in the sign of the mass flux, as the sum of V and III exceeds the buoyancy production at t_2 and t_3.

The discussion above underlies the difficulty of modeling the moments equations for the RTI− case. It has been long recognized in the literature the difficulty of modeling turbulence transients (e.g. [67]). For the current flow, a gradient diffusion hypothesis, popular for this kind of turbulence modeling, clearly cannot represent the mass flux sign change either in time or across the layer. A consistent closure at the second level would include transport equations for both the turbulent mass flux and density specific volume correlation. However, as shown above, the unclosed terms in these equations are also subjected to the transients in the flow behavior, and likely not captured correctly by the current models.

3.6. Vorticity alignment

In the simple turbulent flows extensively studied in the literature (e.g. homogeneous isotropic incompressible and compressible turbulence, simple jets, wakes, and shear driven mixing layers), it is known that vorticity tends to align with the β-strain (intermediate) eigenvector of the strain rate tensor [68]. In the interior of the Rayleigh–Taylor mixing layer, all three (RTI+, RTI−, and RTI0) cases are vorticity dominated (as opposed to strain dominance) and vorticity aligns with the β-strain eigenvector (Fig. 26). Thus, the PDF of the cosine of the angle with the intermediate eigenvector of the strain rate tensor peaks at 1, indicating a most probable distribution towards a zero degree angle. Interestingly, after the gravity reversal, the secondary instabilities still generate enough vorticity to ensure vorticity dominance and maintain the alignment with the strain rate eigenvectors. The PDF of the cosine of the angle with the α-strain eigenvector is almost flat, indicating no preference in the alignment.

In the absence of baroclinic generation of vorticity and the rotation of the principal axes of the strain rate tensor, vorticity tends to align, exponentially fast, with the α-strain eigenvector [68]. The rotation of the principal axes is the only mechanism preventing this alignment in the presence of turbulence. Similar to other turbulent flows, the presence of turbulence leads to a lack of preferential alignment with the α-strain eigenvector. As a consequence, the average of the cosine of the ξ_1 angle is constant across the inner region of the layer, where the rotation of the principal axes of the strain rate tensor remains important. However, over the highly intermittent edge regions, turbulence is not strong enough, the alignment changes, and $\langle cos\xi_1\rangle$ is no longer constant. Thus, the region over which $\langle cos\xi_1\rangle$ is constant can be used as a proxy for the extent of the inner turbulent region of the layer. Figs. 27(a) and (b) show that this region has about the same extent for the RTI+ and RTI0 cases at corresponding

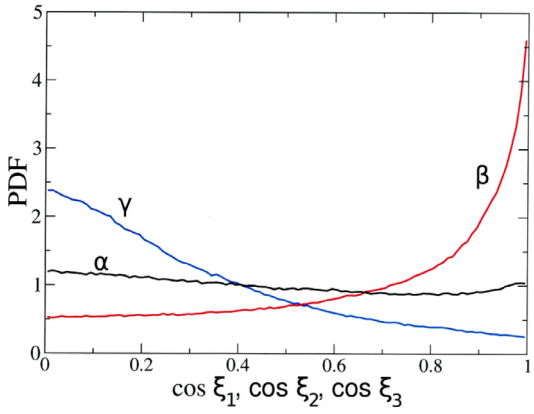

Fig. 26. PDFs of the cosines of the angles, ξ_1, ξ_2, and ξ_3, between the vorticity vector and the eigenvectors of the strain rate tensor for $A = 0.75$ RTI− case at t_3 (see Table 2). The eigenvectors correspond to the eigenvalues α, β, and γ denoted with the usual convention that $\alpha > \beta > \gamma$.

times, even though the layer width based on global considerations changes. However, for the RTI− cases (Fig. 27c), $\langle cos\xi_1 \rangle$ increases significantly near the edges, and the regions where the vorticity alignment follows the turbulent behavior is larger.

4. Conclusions

Results from Direct Numerical Simulations of Rayleigh–Taylor instability are used to investigate the evolution of the flow after the gravity is set to zero or reversed. The simulations cover the range of Atwood numbers $A = 0.5$, 0.75, and 0.9. The $A = 0.04$ results from [19] are also used for comparisons. The branching of the forward simulations is done after the layer growth becomes self-similar. When the gravity is set to zero, the problem becomes anisotropic variable density decaying turbulence and has similarities with the Richmyer–Meshkov instability after re-shock.

As the gravity is reversed, the buoyancy term in the turbulent kinetic energy transport equation, which is given by the product between the mass flux and the mean pressure gradient, changes sign and becomes a destruction term, leading to a rapid decay of the kinetic energy. This is due to a sudden change in sign of the mean pressure gradient contribution, while the mass flux itself maintains the same sign for some time after the gravity reversal. However, the balance of the terms in the mass flux transport equation itself is more complicated and different in the central and edge regions of the mixing layer. In the inner regions, the right hand side of this equation becomes strongly unbalanced and the mass flux reverses sign, so that, certain time after gravity reversal, buoyancy starts producing turbulent kinetic energy again. This process continues with additional mass flux sign changes, leading to transients in the flow evolution both in time and across the layer.

To examine the changes in the turbulence structure after the gravity change, we consider the time instances where the centerline vertical mass flux (a_3) crosses zero or reaches minima and maxima for the corresponding RTI− cases. The results show that a_3 oscillates on a slowly decreasing time scale that becomes shorter with increasing the Atwood number. These oscillations are seen in many of the turbulence moments presented.

For the RTI− cases, by using a definition of the Brünt-Väisällä frequency based on the local mean density, the results show that dimensionaless stratification parameter ($N_{BV}\tau$) is relatively constant across the layer and larger than 1, indicating buoyancy dominance. However, immediately following the gravity reversal, $N_{BV}\tau$ is close to one, a consequence of the violent response of the flow to the sudden change in gravity. Later, it seems to asymptote to a value between 3 and 4. Similar to the stratification parameter, the Ozmidov scale (L_O), is relatively constant in the interior of the layer. For the $A = 0.75$ RTI− simulation, L_O decreases from $\approx 0.22h_b$ at t_0 (corresponding to wavenumber $\kappa = 15$) to $\approx 0.045h_b$ at t_5 (corresponding to wavenumber $\kappa = 75$), so that turbulence becomes restricted to the smallest scales. Within the edge regions of the layer, buoyancy turbulence production still continues throughout the RTI− simulations. However, due to the shape of the mean density profile, which is more elongated on the spike side, so the mean density gradient is smaller, the resulting Ozmidov scale is larger near the spike edge, indicating stronger stratification, relative to turbulence, in this region. Generally, the Elisson scale follows a similar behavior, with values around two times larger than the Ozmidov scale, though there are also differences in the behavior near the edges of the layer.

At the time of the gravity change, the flow is anisotropic both at large and small scales, with an intermediate range of scales where the flow is close to isotropic. After the gravity reversal, the large and small scale anisotropies undergo their own transients, adding another dimension (i.e. the wavenumber in horizontal planes) to the transient processes. The results show that the large scale anisotropy at the centerline oscillates in time but on a longer time scale than the mass flux, while the small scales also exhibit variability, but seem to retain more persistent anisotropy levels. This seems to indicate that gravity reversal mixes more efficiently the larger scales of motion.

On the other hand, density PDFs across the layer show significantly less structure after the gravity reversal, indicating a more efficient mechanism for mixing small scale density fluctuations. Again, this process is asymmetric between the bubble and spike sides, with narrower density PDFs near the spike edge of the mixing layer. Even though the flow undergoes such dramatic changes after the gravity inversion, some turbulence characteristics within the inner region of the layer, for example the alignment between vorticity and strain rate eigenvectors, do not change. This alignment seems to extend even more towards the edges of the layer after the gravity reversal, while the edges remain strongly intermittent and exhibit very different alignment type for the forward and zero gravity cases.

Moreover, while the unclosed terms in the turbulent kinetic energy and mass flux transport equation exhibit complex transients as highlighted above, the mean density profiles still collapse after the change in gravity. Such significant variations in some quantities and not others are difficult to capture with existing turbulence models.

In applications such as ICF, there is a considerable interest in suppressing the evolution of the Rayleigh–Taylor instability. Recent results indicate that time periodic gravity reversals accelerate the suppression of the instability [35]. The transitory behavior for the RTI− case discussed in detail here might indicate that there is an optimal time for a second reversal to maximize the suppression of the instability. Thus, we speculate that the suppression might be faster if the second reversal occurs around or after the time when the mass flux becomes zero. A reversal before this time transforms the buoyancy term from a destruction into a production term for the turbulent kinetic energy transport equation. Subsequent reversals might become more efficient if they are correlated with the sign of the mass flux, instead of at fixed constant intervals.

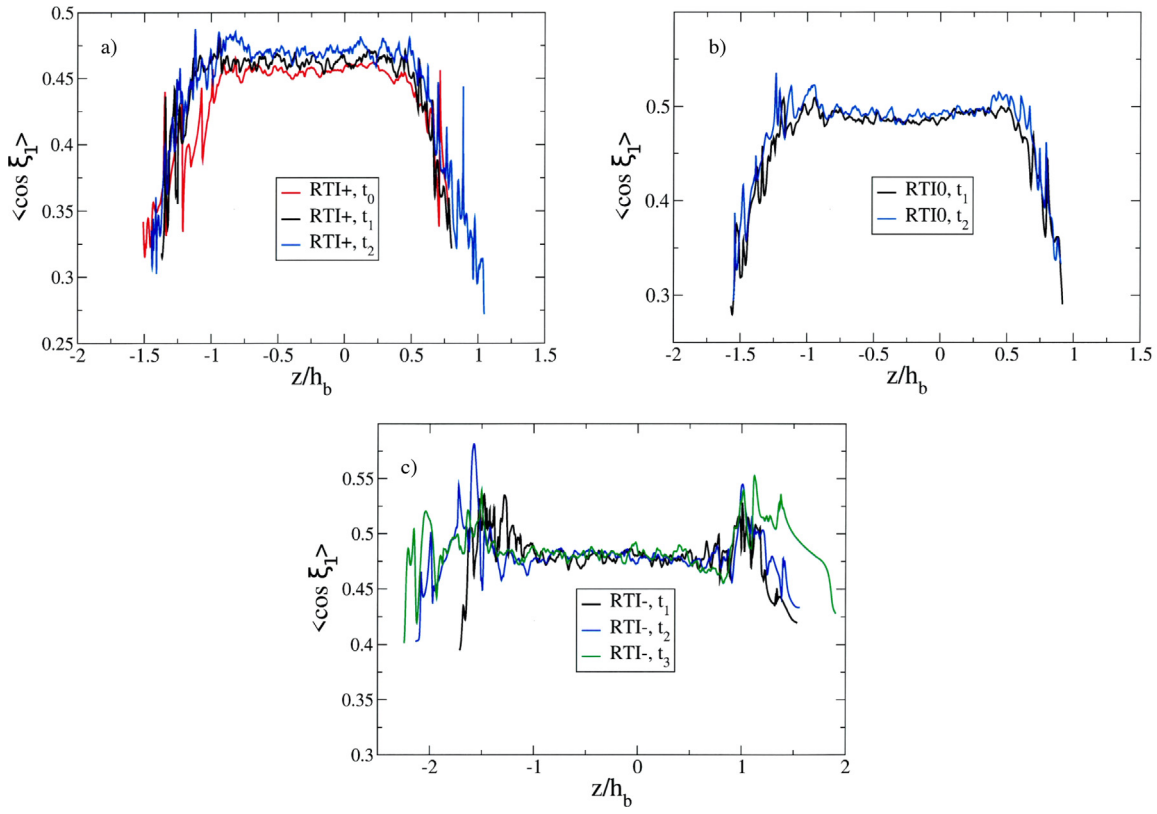

Fig. 27. Vertical variation of the average of $cos\xi_1$ for (a) RTI+, (b) RTI0, and (c) RTI− cases with $A = 0.75$ at different time instants (see Table 2).

CRediT authorship contribution statement

D. Livescu: Conceptualization, Investigation, Formal analysis, Funding acquisition, Methodology, Project administration, Writing - original draft, Writing - review & editing. **T. Wei:** Data curation, Formal analysis, Investigation. **P.T. Brady:** Data curation, Formal analysis, Investigation.

Declaration of competing interest

The authors declare that they have no known competing financial interests or personal relationships that could have appeared to influence the work reported in this paper.

Acknowledgments

This work has been authored by employees of Triad National Security, LLC which operates Los Alamos National Laboratory, USA under Contract No. 89233218CNA000001 with the U.S. Department of Energy/National Nuclear Security Administration. Computational resources were provided at Los Alamos National Laboratory through the Institutional Computing (IC) program and at Lawrence Livermore National Laboratory through the Advanced Simulation and Computation (ASC) program. We are especially grateful to one of the reviewers for detailed and very constructive comments.

References

[1] S. Chandrasekhar, Hydrodynamic and Hydromagnetic Stability, Dover, New York, 1981.
[2] D. Sharp, An overview of Rayleigh–Taylor instability, Physica D 12 (1984) 3–18.
[3] D.L. Youngs, Numerical simulation of turbulent mixing by Rayleigh–Taylor instability, Physica D 12 (1984) 32–44.
[4] W. Cabot, A. Cook, Reynolds number effects on Rayleigh–Taylor instability with possible implications for type-ia supernovae, Nat. Phys. 2 (2006) 562–568.
[5] N.C. Swisher, C.C. Kuranz, D. Arnett, O. Hurricane, B.A. Remington, H.F. Robey, S.I. Abarzhi, Rayleigh–Taylor mixing in supernova experiments, Phys. Plasmas 22 (2015) 102707.
[6] E. Khomenko, A. Diaz, A. de Vicente, M. Collados, M. Luna, Rayleigh–Taylor instability in prominences from numerical simulations including partial ionization effects, Astron. Astrophys. 565 (2014) A45.
[7] S. Gerashchenko, D. Livescu, Viscous effects on the Rayleigh–Taylor instability with background temperature gradient, Phys. Plasmas 23 (2016) 072121.
[8] G. Boffetta, A. Mazzino, Incompressible Rayleigh–Taylor instability, Annu. Rev. Fluid Mech. 49 (2017) 119–143.
[9] F. Ladeindde, Progress in supersonic spray combustion modeling, in: 2018 AIAA Aerospace Sciences Meeting, 2020, p. 0874.
[10] Y. Zhou, Rayleigh–Taylor and Richtmyer-Meshkov instability induced flow, turbulence, and mixing. I, Phys. Rep. 720-722 (2017) 1–136.
[11] Y. Zhou, Rayleigh–Taylor and Richtmyer-Meshkov instability induced flow, turbulence, and mixing. II, Phys. Rep. 723-725 (2017) 1–160.
[12] B.A. Remington, H.S. Park, D.T. Casey, R.M. Cavallo, D.S. Clark, C.M. Huntington, C.C. Kuranz, A.R. Miles, S.R. Nagel, K.S. Raman, V.A. Smalyuk, Rayleigh–Taylor instabilities in high-energy density settings on the national ignition facility, Proc. Natl. Acad. Sci. USA (2018) 1–6.
[13] H. Lin, B. Storey, A. Szeri, Rayleigh–Taylor instability of violently collapsing bubbles, Phys. Fluids 14 (2002) 2925–2928.
[14] D. Livescu, Numerical simulations of two-fluid turbulent mixing at large density ratios and applications to the Rayleigh–Taylor instability, Phil. Trans. R. Soc. A 371 (2013) 20120185.
[15] D. Livescu, Turbulence with large thermal and compositional density variations, Annu. Rev. Fluid Mech. 52 (2020) 309–341.
[16] D.D. Joseph, Fluid dynamics of two miscible liquids with diffusion and gradient stresses, Eur. J. Mech. B/Fluids 6 (1990) 565–596.
[17] D. Livescu, T. Wei, M.R. Petersen, Direct numerical simulations of Rayleigh–Taylor instability, J. Phys.: Conf. Ser. 318 (2011) 082007.
[18] A.W. Cook, P.E. Dimotakis, Transition stages of Rayleigh–Taylor instability between miscible fluids, J. Fluid Mech. 443 (2001) 69–99.
[19] D. Livescu, J.R. Ristorcelli, M.R. Petersen, R.A. Gore, New phenomena in variable-density Rayleigh–Taylor turbulence, Phys. Scr. T 142 (2010) 014015.

[20] T. Wei, D. Livescu, Late-time quadratic growth in single-mode Rayleigh–Taylor instability, Phys. Rev. E 86 (2012) 046405.
[21] W. Cabot, Y. Zhou, Statistical measurements of scaling and anisotropy of turbulent flows induced by Rayleigh–Taylor instability, Phys. Fluids 25 (2013) 015107.
[22] D.L. Youngs, Modelling turbulent mixing by Rayleigh–Taylor instability, Physica D 37 (1989) 270–287.
[23] G. Dimonte, M. Schneider, Density ratio dependence of Rayleigh–Taylor mixing for sustained and impulsive acceleration histories, Phys. Fluids 12 (2000) 304–321.
[24] D. Livescu, J.R. Ristorcelli, Variable-density mixing in buoyancy-driven turbulence, J. Fluid Mech. 605 (2008) 145–180.
[25] D. Livescu, J.R. Ristorcelli, R.A. Gore, S.H. Dean, W.H. Cabot, A.W. Cook, High–Reynolds number Rayleigh–Taylor turbulence, J. Turbul. 10 (2009) 1–32.
[26] A. Banerjee, W.N. Kraft, M.J. Andrews, Detailed measurements of a statistically steady Rayleigh–Taylor mixing layer from small to high Atwood numbers, J. Fluid Mech. 659 (2010) 127–190.
[27] B. Akula, D. Ranjan, Dynamics of buoyancy-driven flows at moderately high atwood numbers, J. Fluid Mech. 795 (2016) 313–355.
[28] R.V. Morgan, O.A. Likhachev, J.W. Jacobs, Rarefaction-driven Rayleigh–Taylor instability. Part 1. Diffuse-interface linear stability measurements and theory, J. Fluid Mech. 791 (2016) 34–60.
[29] R.V. Morgan, W.H. Cabot, J.A. Greenough, J.W. Jacobs, Rarefaction-driven Rayleigh–Taylor instability. Part 2. Experiments and simulations in the nonlinear regime, J. Fluid Mech. 838 (2018) 320–355.
[30] G. Dimonte, P. Ramaprabhu, M. Andrews, Rayleigh-taylor instability with complex acceleration history, Phys. Rev. E 76 (2007) 046313.
[31] V. Zhmaylo, O. Sin'kova, V. Sofronov, V. Statsenko, Y. Yanilkin, A. Guzhova, A. Pavlunin, Numerical study of gravitational turbulent mixing in alternating-sign acceleration, in: B. Cheverushkin, A. Ecer, J. Periaux, N. Satufoka, P. Fox (Eds.), Parallel Computational Fluid Dynamics - Advanced Numerical Methods, Software and Applications, Elsevier, 2004, pp. 235–241.
[32] P. Ramaprabhu, V. Karkhanis, A.G.W. Lawrie, The Rayleigh–Taylor instability driven by an accel-decel-accel profile, Phys. Fluids 25 (2013) 115104.
[33] D. Aslangil, A. Banerjee, A.G.W. Lawrie, Numerical investigation of initial condition effects on Rayleigh–Taylor instability with acceleration reversals, Phys. Rev. E 94 (2016) 053114.
[34] P. Ramaprabhu, V. Karkhanis, R. Banerjee, H. Varshochi, M. Khan, A.G.W. Lawrie, Evolution of the single-mode rayleigh-taylor instability under the influence of time-dependent accelerations, Phys. Rev. E 93 (2016) 013118.
[35] G. Boffetta, M. Magnani, S. Musacchio, Suppression of rayleigh-taylor turbulence by time-periodic acceleration, Phys. Rev. E 99 (2019) 033110.
[36] D. Livescu, T. Wei, Direct numerical simulations of Rayleigh–Taylor instability with gravity reversal, in: Proceedings of the Seventh International Conference on Computational Fluid Dynamics (ICCFD7), Big Islannd, HI, 2012, July 9-13, 2012, p. paper number 2304.
[37] D. Sandoval, The Dynamics of Variable Density Turbulence, LANL report LA-13037-T, Ph.D. thesis, University of Washington, 1995.
[38] A. Majda, J. Sethian, The derivation and numerical solution of the equations for zero Mach number combustion, Combust. Sci. Tech. 42 (1985) 185–205.
[39] D. Chung, D.I. Pullin, Direct numerical simulation and large-eddy simulation of stationary buoyancy-driven turbulence, J. Fluid Mech. 643 (2010) 279–308.
[40] S.K. Lele, Compact finite difference schemes with spectral-like resolution, J. Comput. Phys. 103 (1992) 16–42.
[41] J. Mohd-Yusof, D. Livescu, T.M. Kelley, Adapting the CFDNS compressible Navier–Stokes solver to the Roadrunner architecture, in: R. Biswas (Ed.), Parallel Computational Fluid Dynamics, Recent Advances and Future Directions, DESTech Publications, Lancaster, PA, 2010, pp. 95–109.
[42] R.E. Duff, F.H. Harlow, C.W. Hirt, Effects of diffusion on interface instability between gases, Phys. Fluids 5 (1962) 417–425.
[43] J.D. Schwarzkopf, D. Livescu, J.R. Baltzer, R.A. Gore, J.R. Ristorcelli, A two length-scale turbulence model for single-phase multi-fluid mixing, Flow Turbul. Combust. 96 (2016) 1–43.
[44] I.W. Kokkinakis, D. Drikakis, D.L. Youngs, Modeling of Rayleigh–Taylor mixing using single-fluid models, Phys. Rev. E 99 (2019) 013104.
[45] M. Andrews, D. Spalding, A simple experiment to investigate two-dimensional mixing by Rayleigh–Taylor instability, Phys. Fluids A 2 (1990) 922–927.
[46] D. Youngs, Three-dimensional numerical simulation of turbulent mixing by Rayleigh–Taylor instability, Phys. Fluids A 3 (1991) 1312–1320.
[47] D. Youngs, Numerical simulation of mixing in Rayleigh–Taylor and Richtmyer-Meshkov instabilities, Laser Part. Beams 12 (1994) 725–750.
[48] D. Youngs, Application of monotone integrated large eddy simulation to Rayleigh–Taylor mixing, Phil. Trans. R. Soc. A 367 (2009) 2971–2983.
[49] D.L. Youngs, Rayleigh–Taylor mixing: direct numerical simulation and implicit large eddy simulation, Phys. Scr. 92 (2017) 074006.
[50] B.-J. Grea, The rapid acceleration model and the growth rate of a turbulent mixing zone induced by rayleigh-taylor instability, Phys. Fluids 25 (2013) 015118.
[51] B.E. Morgan, B.J. Olson, W.J.E., J.A. MacFarland, Self-similarity of a rayleigh–taylor mixing layer at low atwood number with a multimode initial perturbation, J. Turbul. 18 (2017) 973–999.
[52] D.L. Youngs, The density ratio dependence of self-similar rayleigh–taylor mixing, Phil. Trans. R. Soc. A 371 (2013) 20120173.
[53] G. Dimonte, et al., A comparative study of the turbulent Rayleigh–Taylor instability using high-resolution three-dimensional numerical simulations: The alpha-group collaboration, Phys. Fluids 16 (2004) 1668–1692.
[54] J. Ristorcelli, T. Clark, Rayleigh–Taylor turbulence: Self-similar analysis and direct numerical simulations, J. Fluid Mech. 507 (2004) 213–253.
[55] K.I. Read, Experimental investigation of turbulent mixing by Rayleigh–Taylor instability, Physica D 12 (1984) 45–58.
[56] D.H. Olson, J.W. Jacobs, Experimental study of Rayleigh–Taylor instability with a complex initial perturbation, Phys. Fluids 21 (2009) 034103.
[57] M.S. Roberts, J.W. Jacobs, The effects of forced small-wavelength, finite-bandwidth initial perturbations and miscibility on the turbulent Rayleigh–Taylor instability, J. Fluid Mech. 787 (2016) 50–83.
[58] C.R. Weber, A.W. Cook, R. Bonazza, Growth rate of a shocked mixing layer with known initial perturbations, J. Fluid Mech. 725 (2013) 372–401.
[59] M.L. Wong, D. Livescu, S.K. Lele, High-resolution Navier–Stokes simulations of Richtmyer-Meshkov instability with re-shock, Phys. Rev. Fluids 4 (2019) 104609.
[60] V.K. Tritschler, B.J. Olson, S.K. Lele, S. Hickel, X. Hu, N.A. Adams, On the Richtmyer–Meshkov instability evolving from a deterministic multimode planar interface, J. Fluid Mech. 755 (2014) 429–462.
[61] B. Thornber, D. Drikakis, D.L. Youngs, R.J.R. Williams, Growth of a Richtmyer–Meshkov turbulent layer after reshock, Phys. Fluids 23 (2011) 095107.
[62] O. Soulard, J. Griffond, B.-J. Grea, Influence of the mixing parameter on the second order moments of velocity and concentration in Rayleigh–Taylor turbulence, Phys. Fluids 28 (2016) 065107.
[63] A. Briard, M. Iyer, T. Gomez, Anisotropic spectral modeling for unstably stratified homogeneous turbulence, Phys. Rev. Fluids 42 (2017) 044604.
[64] A. Briard, B.-J. Grea, L. Gostiaux, Harmonic to subharmonic transition of the Faraday instability in miscible fluids, Phys. Rev. Fluids 4 (2019) 044502.
[65] D. Zhao, H. Aluie, Inviscid criterion for decomposing scales, Phys. Rev. Fluids 3 (2018) 054603.
[66] D. Aslangil, D. Livescu, A. Banerjee, Effects of Atwood and Reynolds numbers on the evolution of buoyancy-driven homogeneous variable-density turbulence, J. Fluid Mech. 895 (2020) A12.
[67] B.-J. Grea, A. Burlot, J. Griffond, A. Llor, Challenging mix models on transients to self-similarity of unstably stratified homogeneous turbulence, ASME J. Fluids Eng. 138 (2016) 070904.
[68] W.T. Ashurst, A.R. Kerstein, R.M. Kerr, C.H. Gibson, Alignment of vorticity and scalar gradient with strain rate in simulated Navier–Stokes turbulence, Phys. Fluids 30 (1987) 2343–2353.